Journal of African Earth Sciences 197 (2023) 104738

Contents lists available at ScienceDirect

Journal of African Earth Sciences

journal homepage: www.elsevier.com/locate/jafrearsci

Reconstruction of magma chamber processes preserved in olivine-phlogopite micro-ijolites from the Oldoinyo Lengai, Tanzania

Noémi Halász [a], Márta Berkesi [b,c], Tivadar M. Tóth [a], Roger H. Mitchell [d], Ralf Milke [e], Tibor Guzmics [b,*]

[a] Department of Mineralogy, Geochemistry and Petrology, University of Szeged, 6722 Szeged, Egyetem utca 2-6, Hungary
[b] Lithosphere Fluid Research Laboratory, Institute of Geography and Earth Sciences, Eötvös Loránd University, Pázmány Péter stny. 1/C, 1117, Budapest, Hungary
[c] Institute of Earth Physics and Space Science, Eötvös Loránd Research Network (ELKH) 1112 Budapest, Meredek utca 18, Hungary
[d] Department of Geology, Lakehead University, Thunder Bay, ON P7B 5E1, Canada
[e] Freie Universität Berlin, Malteserstr. 74-100, 14195, Berlin, Germany

ARTICLE INFO

Keywords:
Ijolite
Double corona microtexture
Symplectite
Clinopyroxene zonation
Oldoinyo lengai

ABSTRACT

A detailed petrographic and mineralogical investigation of olivine-phlogopite micro-ijolite xenoliths from Oldoinyo Lengai, Tanzania indicates a complex evolutional history. These xenoliths consist of diverse textural subdomains characterized by minerals ranging from early-formed olivine, through diopside-hosted perovskite and phlogopite, to evolved aegirine-augite and titanite. Thermometry and mineral compositions in the subdomains suggest crystallization temperatures from 1070–970 °C to 850–700 °C at plutonic pressures and SiO_2-activities controlled by perovskite-titanite equilibria. Double coronas are a characteristic textural feature of the olivine-phlogopite micro-ijolite, consisting of olivine cores surrounded by an inner clinopyroxene corona and an outer phlogopite corona. These double coronas might have formed during early magma chamber processes, including magma movement to a subsequent chamber resulting in dissolution of olivine with subsequent crystallization and accumulation of diopside and phlogopite. Diopside−aegirine-augite compositional zonation indicates several magma injections followed by cooling periods, during the formation of micro-ijolite groundmass. Mg# (80–83) and Ca (0.1–0.3 in wt%) contents of olivine together with the presence of primary melt inclusions in clinopyroxene, phlogopite, and nepheline indicate a magmatic origin from a possible parental olivine-nephelinite melt. There is evidence for subsolidus, or near-solidus, re-equilibration processes as indicated by the reaction of olivine with titanite forming symplectitic textures of ilmenite and diopside with minor zirconolite. Ti-exchange between phlogopite phenocrysts and other Ti-bearing minerals (perovskite, titanite, magnetite) resulted in ~750 °C equilibrium temperatures for phlogopite, which are much lower than mafic magmatic (>900 °C) conditions. Calculated subsolidus temperatures suggest crystallization of olivine-phlogopite micro-ijolites over a 10–20 km depth interval.

1. Introduction

Oldoinyo Lengai (Tanzania) is the only known active carbonatite volcano (Dawson, 2008), and is unique due to the eruption of natro-carbonatite lavas (Yaxley et al., 2022). It is special not only because of the composition of the lava but also the xenoliths it brings to the surface. The wide spectrum of different pyroxenites, nephelinolites (urtite, ijolite, etc.) indicate a complex composition and evolution beneath the volcanic region. On the basis of previous studies, olivine-phlogopite ijolites are among the xenoliths with the most complex petrography (Keller and Krafft, 1990; Dawson et al., 1995; Dawson, 2008; Carmody, 2012; Sekisova et al., 2015). This rare ijolite type consists of large phlogopite phenocrysts and olivine xenocrysts surrounded by double coronas in addition to nepheline and diopside (Dawson et al., 1995; Dawson, 2008; Carmody, 2012; Sekisova et al., 2015). Olivine-phlogopite ijolites probably represent several steps in their evolution as recorded by the different textures, which can be utilized to reconstruct magma chamber processes.

In this investigation petrographic and mineral compositional data of a selected olivine-phlogopite ijolite xenolith from Oldoinyo Lengai are

* Corresponding author.
E-mail address: tibor.guzmics@gmail.com (T. Guzmics).

https://doi.org/10.1016/j.jafrearsci.2022.104738
Received 21 April 2022; Received in revised form 8 August 2022; Accepted 27 September 2022
Available online 30 September 2022

evaluated in conjunction with previous investigations of similar xenoliths literature information representing the same (Dawson and Smith, 1992a; Dawson et al., 1995; Carmody, 2012; Sekisova et al., 2015). We emphasize our evolutionary model for these olivine-phlogopite ijolite xenoliths is based on our own research together with investigations by the above cited authors on similar xenoliths.

2. Background

2.1. Regional geology

The East African Rift System splits the African plate into the Nubian and the Somalian plates along the two main rift branches, the Western Rift and the Eastern Rift. The Eastern Rift lies between the Tanzania craton and the Mozambique orogenic fold belt (Dawson, 2008) (Fig. 1). The Tanzania craton is a composite of Archean metasediments and is composed of greenstone belts (Pinna et al., 1995) intruded by granite plutons (Cahen et al., 1984). The lithologically very complex Mozambique belt formed as part of the Pan African orogeny (Kennedy, 1964).

On the basis of gravity anomaly data (Ebinger and Sleep, 1998; Rogers et al., 2000), it is considerd that plate motion is possibly governed by one or more impinging mantle plumes beneath the region. These plumes have also resulted in lithospheric thinning and a high geothermal gradient along the rift, such as ~65 °C/km in southeastern Kenya and northeastern Tanzania. Oldoinyo Lengai is located in northern Tanzania, in the southern part of the Eastern Rift, where a lower geothermal gradient of ~40 °C/km prevails (Brown and Girdler, 1980; Nyblade, 1997; Simiyu and Keller, 1997). This anomaly can be explained by the presence of the brittle, relatively cool Tanzania craton (Fig. 1).

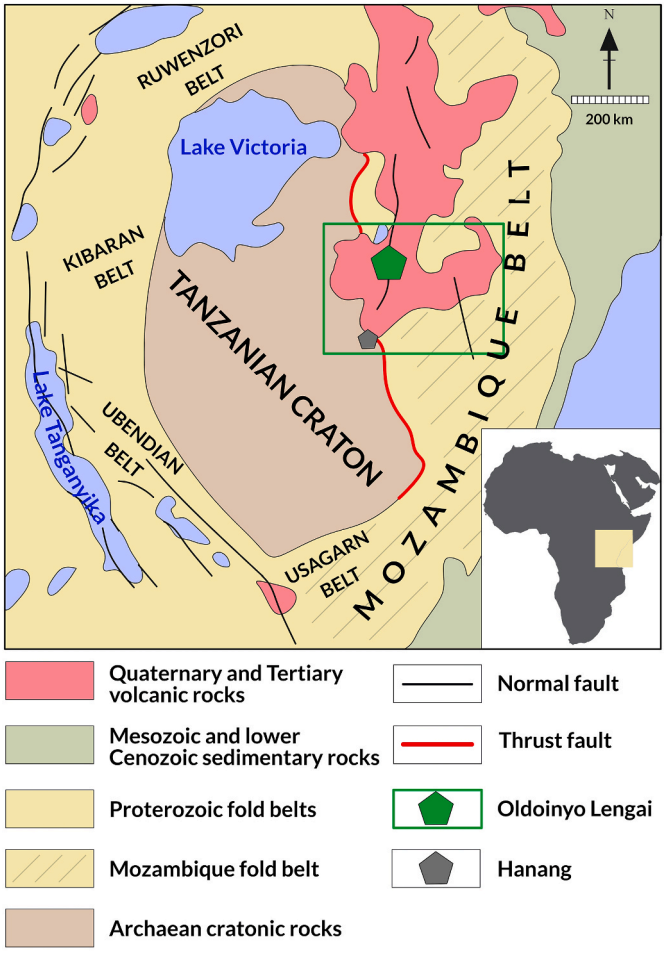

Fig. 1. Geological map of the region, showing the main tectonical and geological structures and the location of the Oldoinyo Lengai volcano.

Oldoinyo Lengai is located in the North Tanzanian Divergence and is part of the Tanzanian volcanic province. Each but the Hanang volcano in this area (e.g., Oldoinyo Lengai, Kerimasi, etc.) has erupted through the Mozambique belt (Quennell et al., 1956) (Fig. 1). The lithosphere beneath the North Tanzanian Volcanic Province is structurally and lithologically extremely heterogeneous (Dawson, 2008). Previous studies indicate that the lithosphere (upper mantle, lower cratonic lithosphere) has been intensively metasomatized in many parts of the rift (Lloyd and Bailey, 1975; Norry et al., 1980; Clement, 1982; Dawson and Smith, 1988; Dawson and Smith, 1992a,b; Dawson, 1999; Dawson, 2002; Dawson, 2012), as indicated by phlogopite- and clinopyroxene-bearing veins cross-cutting mantle xenoliths (Wölbern et al., 2012).

2.2. Ijolites from Oldoinyo Lengai

Ijolites are common plutonic rocks in alkali-silicate-carbonatite complexes worldwide (Woolley et al., 1995; Pilipiuk et al., 2001; Woolley and Church, 2005; Haslinger et al., 2007; Woolley and Kjarsgaard, 2008; Zurevinski and Mitchell, 2015; Beccaluva et al., 2017; Savard and Mitchell, 2021). At Oldoinyo Lengai, the most common plutonic rocks are pyroxenite, urtite and ijolite, occurring as blocks or bombs hosted by nephelinite lavas and pyroclasts (Dawson, 2008). Oldoinyo Lengai ijolites can be divided into two distinct types: archetypal coarse grained plutonic ijolite (consisting of clinopyroxene, nepheline, titanite, magnetite, perovskite, biotite, ±garnet, ±wollastonite) and olivine-phlogopite ijolite (clinopyroxene, nepheline, titanite, magnetite, perovskite, biotite, ±garnet, ±wollastonite, phlogopite and olivine) (Dawson et al., 1995; Dawson, 2008; Sekisova et al., 2015). The latter, although they have the typomorphic assemblage of nepheline and pyroxene cannot be usefully termed ijolite *sensu stricto* as they are texturally different and do not exhibit the typical allotriomorphic granular textures of plutonic ijolites. We believe that there was not enough time for recrystallization to develop a typical allotriomorphic texture, probably because due to a volcanic eruption the xenolith left its original place and was either brought to an upper place or even to the surface before this textural feature could be formed. In addition, they cannot be described as nephelinites as they are not eruptive rocks. In other settings the xenoliths, on a textural basis, would be classified as hypabyssal facies rocks. There is currently no IUGS approved term for this fine-to-coarse-grained assemblage but terming them ijolite sensu stricto leads to inappropriate petrogenetic comparisons with the plutonic varieties. There is no petrological reason to perpetuate the name ijolite as used by Dawson et al. (1995) and to this end; we propose that these distinctive xenoliths be termed *olivine--phlogopite micro-ijolite xenoliths.*

The olivine-phlogopite micro-ijolite xenoliths investigated have similarities with those occurring in the 1966 eruptions. In the activity of 1966, ijolites usually occurred by clinopyroxenes, nepheline, micas, olivine, titanite, magnetite and perovskite. The properties of the volcanic rock enclosing these ijolites also support the similarity with the 1966 rocks. The volcanic rocks of the 1966 eruptions contain melanite, nepheline, wollastonite, clinopyroxene (Dawson et al., 1995).

All xenoliths and particularly olivine-phlogopite micro-ijolites of complex petrography carry essential information regarding magma chamber processes. Previously, Sekisova et al. (2015) found that olivine-phlogopite micro-ijolites consist of a groundmass of nepheline, clinopyroxene (alternate diopside and aegirine-augite zones), apatite, Ti-magnetite, perovskite, sulphides, titanite and Ti-andradite. They identified phlogopite phenocrysts (Mg# = 84) with biotite rims (Mg# = 63–76) and double coronas with olivine (Mg# = 79–85) in the core, surrounded by an inner clinopyroxene and an outer phlogopite corona. Dawson et al. (1995) studied jacupirangite, ijolite and

olivine-phlogopite micro-ijolite xenoliths. The latter have a similar mineral paragenesis and composition to those investigated by Sekisova et al. (2015), with the presence of phlogopite phenocrysts (Mg# = 84–86) with a biotite rim (Mg# = 61–74) and double coronas. Carmody (2012) describes very similar ijolites with olivine, double coronas, and phlogopite with biotite rims. Dawson and Smith (1992) examined pyroxenites, which contained resorbed olivine (Mg# = 73–83) crystals with a double corona (light green coloured clinopyroxene corona and a brownish mica corona). They also noted the presence of phlogopite phenocrysts (Mg# = 80–86), but without biotite rims. The multistage evolution of these rocks has been interpreted in diverse ways. On the basis of these models, olivine crystals with common resorbed rims might represent subcontinental mantle, which has undergone mantle metasomatism (Dawson and Smith, 1988, 1992a; Dawson et al., 1995; Sekisova et al., 2015). Keller et al. (2006) and Baudouin and Parat (2020) have suggested that Oldoinyo Lengai olivines are early crystallization products from a primitive silicate magma. Olivine crystals are typically surrounded by a double corona microtexture. The inner corona contains clinopyroxene whereas the outer contains mica. The clinopyroxene corona is considered to have formed by reaction between olivine and the alkaline magma (Dawson et al., 1995; Sekisova et al., 2015), whereas the outer mica corona might be the result of a similar reaction or a metasomatic product (Dawson and Smith, 1992b). The phlogopites from the North Tanzanian divergence probably originated from phlogopite-bearing veins that commonly crosscut the deep crust (Wölbern et al., 2012). Clement (1982), Dawson and Smith (1992a,b) and Kargin et al. (2019) have suggested that the phlogopites of the region are fragments of metasomatized mantle rocks, whereas Baudouin and Parat (2020) suggest a magmatic origin.

3. Sampling and methods

We collected numerous ijolite xenoliths from pyroclasts on the northern slope of Oldoinyo Lengai (~longitude: 2.749002, ~latitude: 35.890602) and randomly choose five samples for detailed investigation. All xenoliths exhibited the same texture and mineral paragenesis. Consequently, we selected one representative sample to investigate in detail. This research focuses not only on such sample, but includes commentary on previously published data for similar olivine-phlogopite micro-ijolites (Dawson and Smith, 1992a, b; Dawson et al., 1995; Sekisova et al., 2015; Carmody, 2012).

Petrographic observations were undertaken in the Department of Mineralogy, Geochemistry and Petrology of the University of Szeged using Brunel- SP -300-P and Olympus BX 41 optical microscopes. Major element compositions of the rock-forming minerals and silicate glass were determined using a JEOL JXA 8200 Superprobe with five wavelength dispersive spectrometers at the Free University Berlin with instrument settings of 15 kV accelerating voltage and 20 nA beam current. The glass was analyzed with a 10 μm diameter beam, whereas a 2 μm diameter was found to be sufficient for minerals. Ilmenite and zirconolite compositions were measured by a Quantax75 EDS-SDD combined with a Hitachi TM4000Plus microscope at the ELTE FS-RICF with instrument settings of 15 kV accelerating voltage, 833 pA beam current, and 15 s counting times. Natural standards were used for instrument calibration, and full ZAF corrections were applied.

4. Petrography and mineral compositions

The sample investigated consists of an olivine-phlogopite micro-ijolite xenolith (Fig. 2A) mantled by nephelinite (Fig. 2B). At the contact, there is a well-defined, 400 μm wide aegirine-augite zone with oriented prismatic crystals of clinopyroxene (Fig. 2C and Table 1).

4.1. Olivine-phlogopite micro-ijolite

The groundmass of the olivine-phlogopite micro-ijolite xenolith is medium-grained (0.05–2 mm) and consists of clinopyroxene, nepheline, minor titanite, and pseudomorphic analcime (Fig. 3A). Clinopyroxene occurs as either zoned euhedral (Fig. 3A) or anhedral phenocrysts; the latter having corroded margins (Fig. 3B). The colour of the groundmass clinopyroxene ranges from light-to-dark green (Fig. 3A and B) and from dark green-to-light green. The light green material is diopside (Mg# = 86–98) with (all in wt%) 14.7–15.5 MgO, 4.8–5.5 FeO^T, 0.4–0.6 Na_2O (Table 1). The dark green zone is aegirine-augite (Mg# = 58–80) enriched in (all in wt%) Na_2O (3.4–4.0), FeO^T (16.6–17.9) and depleted in MgO (7.4–8.4) compared to the diopside (Table 1). The diopside zones are rich in fine-grained (50 μm) euhedral inclusions of magnetite and perovskite (Fig. 3C) (Table 2), whereas the aegirine-augite zones host inclusions of titanite (Fig. 3D). Both zones host randomly distributed primary melt inclusions (Fig. 3D). Nepheline is euhedral (Fig. 3A), homogeneous in composition, and contains 1.2–2.1 wt% FeO^T (Table 3). It also hosts randomly distributed clinopyroxene and melt inclusions. Titanite occurs as either large (~1 mm) subhedral crystals with magnetite and perovskite inclusions (Fig. 3E) or anhedral crystals with fewer mineral inclusions (Fig. 3F). All titanites are homogeneous in composition and contain small amounts of ZrO_2 (0.4–0.8 wt%) and FeO

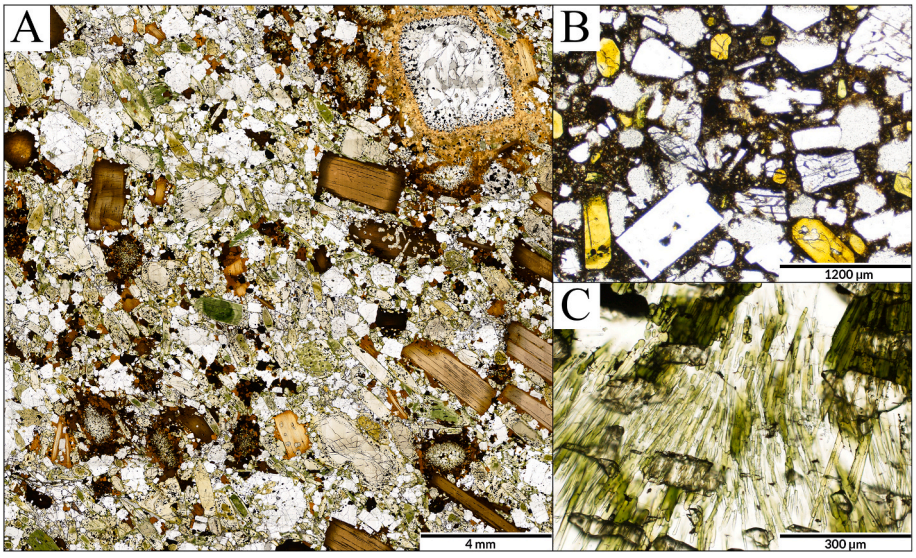

Fig. 2. Representative petrographic images of the sample. (A) The olivine-phlogopite micro-ijolite xenolith; (B) the host nephelinite; (C) the contact zone.

Table 1
Representative composition (wt%) of clinopyroxene and olivine from the olivine-phlogopite micro-ijolite, Oldoinyo Lengai, Tanzania. FeO^T: all Fe as FeO; mg#: Mg/(Mg + Fe^{II}), molar, b.d.: below the detection limit; WDS: Wavelength Dispersive Spectrometry.

	Ijolite																										
	clinopyroxene (WDS)																								**olivine (WDS)**			
	ijolite matrix								***ijolite-nephelinite contact***			***double corona***								***symplectite***				***double corona***			
	diopside zone				*aegirine-augite zone*				*aegirine-augite*			*diopside*				*augite*				*diopside*							
SiO_2	51.63	50.29	51.94	51.12	50.22	51.28	51.34	50.80	51.23	51.45	50.43	54.40	54.50	49.41	54.47	52.65	53.09	51.24	52.72	53.54	50.35	52.24	51.87	38.91	38.58	38.72	38.60
TiO_2	1.12	1.54	1.09	1.60	0.41	0.78	0.66	0.66	1.74	0.89	1.74	0.29	0.25	4.41	0.27	0.61	0.33	0.60	0.44	1.05	4.43	1.49	1.59	b.d.	0.01	b.d.	b.d.
Al_2O_3	1.03	2.07	0.86	1.63	1.05	0.91	0.79	0.90	1.40	1.07	1.47	0.11	0.09	0.14	0.12	0.60	0.50	0.71	0.62	0.24	0.24	1.30	1.27	0.04	0.03	0.02	0.02
FeO^T	4.86	5.30	3.98	5.01	19.33	17.23	16.63	17.40	13.21	13.51	13.68	3.86	4.55	6.97	4.66	13.23	11.99	12.80	12.18	5.99	7.71	4.19	5.27	16.44	19.39	17.54	16.63
Cr_2O_3	b.d.	0.01	b.d.	0.06	0.02	0.07	0.04	0.07	b.d.	b.d.	b.d.	b.d.	b.d.	0.04	b.d.	b.d.	b.d.	0.07	b.d.	b.d.	b.d.	b.d.	b.d.	b.d.	b.d.	0.01	0.01
MnO	0.11	0.06	0.05	0.06	0.30	0.18	0.18	0.23	0.37	0.40	0.38	0.18	0.11	0.11	0.36	0.51	0.38	0.21	0.40	0.12	0.52	0.13	0.22	0.13	0.45	0.27	0.25
MgO	15.49	14.73	15.75	15.38	6.39	7.98	8.43	8.01	9.68	9.75	9.25	16.82	16.36	14.89	16.48	10.63	11.17	10.57	11.13	15.17	15.29	16.64	15.79	44.80	42.25	44.25	44.75
NiO	b.d.	b.d.	b.d.	b.d.	b.d.	b.d.	b.d.	b.d.	b.d.	b.d.	b.d.	b.d.	b.d.	b.d.	b.d.	b.d.	b.d.	b.d.	b.d.	b.d.	b.d.	b.d.	b.d.	b.d.	b.d.	b.d.	b.d.
SrO	0.03	0.06	0.06	0.01	0.06	0.02	0.05	0.03	0.10	0.12	0.13	b.d.	b.d.	0.11	0.02	b.d.	0.24	0.08	0.12	0.11	b.d.	b.d.	b.d.	0.02	b.d.	b.d.	b.d.
CaO	25.16	24.67	24.88	24.44	19.04	17.74	17.60	17.32	20.21	20.90	19.96	23.57	23.15	22.52	22.72	18.59	19.60	20.58	19.77	22.45	20.14	23.44	23.35	0.25	0.13	0.15	0.16
Na_2O	0.41	0.49	0.45	0.62	2.90	3.42	3.56	3.74	2.55	2.44	2.64	0.77	1.00	0.79	0.91	3.18	2.69	2.18	2.62	1.31	1.35	0.57	0.64	b.d.	b.d.	b.d.	b.d.
Total	99.83	99.21	99.05	99.94	99.73	99.59	99.28	99.14	100.50	100.50	99.67	100.00	100.01	99.39	100.01	100.00	99.99	99.03	100.00	99.98	100.03	100.00	100.00	100.58	100.83	100.94	100.42
formula based on: 4 cations and 6 oxygens																								3 cations and 4 oxygens			
Si	1.906	1.863	1.911	1.860	1.950	1.972	1.947	1.918	1.926	1.938	1.939	1.959	1.975	1.846	1.996	1.979	1.960	1.928	1.977	1.980	1.906	1.863	1.911	0.980	0.983	0.977	0.975
Ti	0.031	0.043	0.030	0.044	0.012	0.022	0.019	0.019	0.049	0.025	0.050	0.008	0.007	0.124	0.007	0.017	0.009	0.017	0.012	0.029	0.031	0.043	0.030	–	–	–	0.001
Al^{IV}	0.045	0.090	0.037	0.070	0.038	0.006	0.034	0.040	0.025	0.037	0.011	0.005	0.004	0.006	–	0.004	0.022	0.032	0.011	–	0.045	0.090	0.037	0.001	0.001	0.000	0.001
Al^{VI}	–	–	–	–	0.010	0.035	0.001	–	0.038	0.011	0.056	–	–	–	0.009	0.022	–	–	0.016	0.019	–	–	–	–	–	–	–	–
Fe^{II}	0.029	0.040	0.027	0.026	0.352	0.292	0.243	0.230	0.234	0.202	0.229	0.039	0.054	0.115	0.070	0.172	0.176	0.197	0.176	0.089	0.029	0.040	0.027	0.346	0.413	0.370	0.351
Fe^{III}	0.121	0.124	0.095	0.127	0.276	0.262	0.285	0.319	0.181	0.224	0.211	0.078	0.084	0.103	0.073	0.244	0.194	0.206	0.206	0.096	0.121	0.124	0.095	–	–	–	–
Cr	–	0.000	–	0.002	0.001	0.002	0.001	0.002	–	–	–	–	–	0.001	–	–	–	0.002	–	–	–	–	–	–	–	0.000	0.000
Mn	0.003	0.002	0.001	0.002	0.010	0.006	0.006	0.007	0.012	0.012	0.012	0.005	0.003	0.004	0.011	0.016	0.012	0.007	0.013	0.004	0.003	0.002	0.001	0.003	0.010	0.006	0.005
Mg	0.852	0.814	0.864	0.834	0.370	0.457	0.477	0.451	0.543	0.548	0.530	0.903	0.884	0.829	0.900	0.596	0.615	0.593	0.622	0.836	0.852	0.814	0.864	1.682	1.605	1.665	1.685
Sr	0.001	0.001	0.001	–	0.001	0.001	0.001	0.001	0.002	0.003	0.003	0.000	0.000	0.002	0.000	0.000	0.005	0.002	0.003	0.002	0.001	0.001	0.001	0.000	0.000	0.000	–
Ca	0.995	0.979	0.981	0.953	0.792	0.731	0.715	0.700	0.814	0.814	0.822	0.909	0.899	0.901	0.892	0.748	0.775	0.829	0.794	0.889	0.995	0.979	0.981	0.007	0.003	0.004	0.004
Na	0.029	0.035	0.032	0.044	0.218	0.255	0.262	0.273	0.186	0.178	0.197	0.054	0.070	0.057	0.065	0.232	0.193	0.159	0.190	0.094	0.029	0.035	0.032	0.000	0.000	0.000	–
Sum	4.012	3.991	3.982	3.961	4.030	4.039	3.991	3.959	4.011	4.018	4.058	3.962	3.982	3.991	4.018	4.029	3.961	3.972	4.019	4.035	4.012	3.991	3.983	3.019	3.016	3.023	3.022
mg#	97	95	97	97	51	61	66	66	70	73	70	96	94	88	93	78	78	75	78	90	86	96	93	83	80	82	83

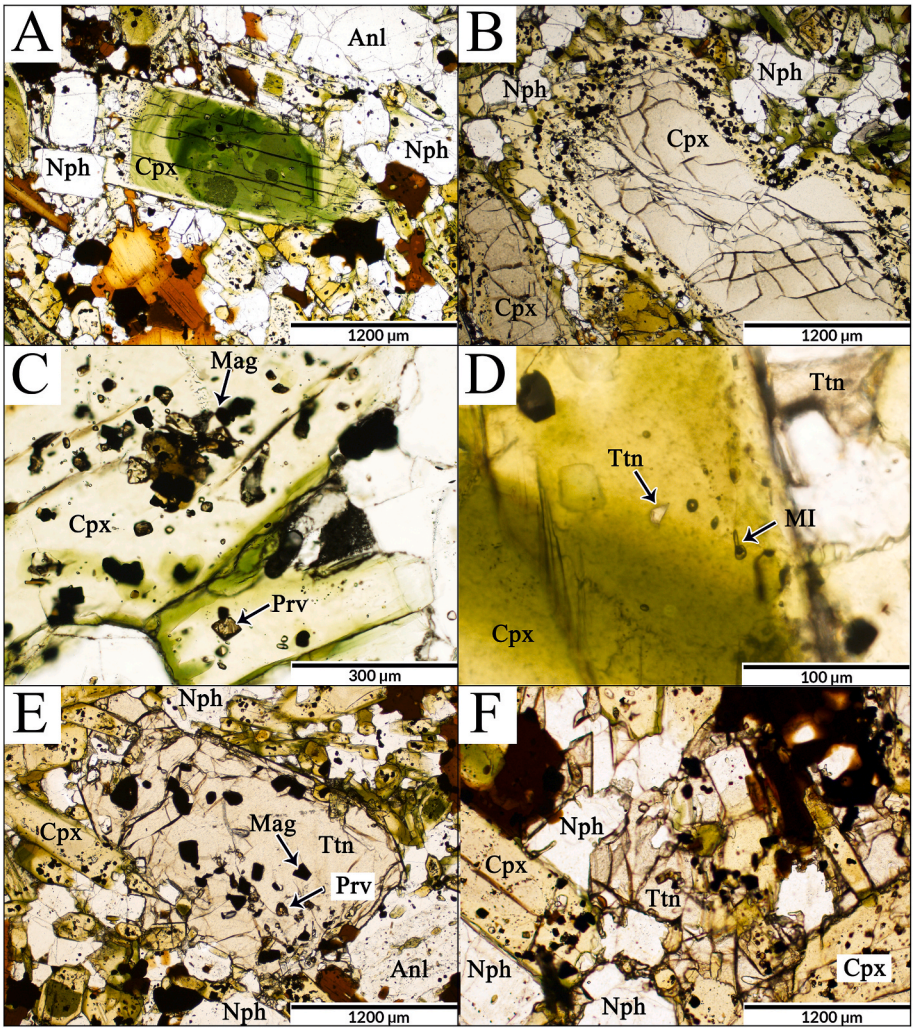

Fig. 3. Petrographic images of the groundmass of olivine-phlogopite micro-ijolite xenolith, Oldoinyo Lengai, Tanzania. (A) euhedral and zoned clinopyroxene with associated minerals; (B) clinopyroxene with a corroded margin; (C) perovskite and magnetite inclusions in the diopside zone; (D) titanite and primary melt inclusions enclosed by aegirine-augite; (E) euhedral titanite with magnetite and perovskite inclusions; (F) anhedral titanite with groundmass minerals. Abbreviations (Whitney and Evans, 2010): Cpx – clinopyroxene, Nph – nepheline, Anl – analcime, Prv – perovskite, Mag – magnetite, Ttn – titanite, MI – melt inclusion.

(1.6–2.2 wt%) (Table 3).

The groundmass contains larger oriented and euhedral light brown phlogopite phenocrysts (Mg# = 81–85) (Fig. 4A–F), up to 5 mm in size, containing (all in wt%) 4.7–5.4 TiO_2, 0.1–0.2 BaO, and 0.6–1 F (Table 3); the water content is estimated to be 3.4–3.7 wt%. Phlogopite encloses magnetite, perovskite, apatite (Fig. 4B), and diopside (Fig. 4C) plus randomly distributed primary melt inclusions (~20 μm, Fig. 4D). The phenocrysts commonly exhibit kink bands (Fig. 4E). All phlogopites have dark brown anhedral rims (Fig. 4A, E and F) of biotite (Mg# = 55–61) containing 3.2–4.2 wt% TiO_2 and 0.1–0.3 wt% BaO, 0.6–0.7 wt % F (Table 3); the water content is estimated to be 3.8–4.8 wt%. The rim hosts numerous inclusions of groundmass minerals (Fig. 4A, E and F). The orientation of clinopyroxene from the groundmass (n = 390) together with the phlogopite phenocryst (n = 62) was measured using the relative tilt angle of the grains. Both the mica phenocrysts and that of the groundmass have the same orientation.

An important aspect of the xenolith is the double corona. Olivine xenocrysts, up to 2 mm in size, are found at the centre of such coronas (Fig. 5A and B), with the exception of smaller (<1.5 mm) coronas in which olivine was not observed (Fig. 5C). Olivine (Mg# = 80–83) is homogeneous in composition with CaO and MnO contents of 0.1–0.3 and 0.1–0.5 wt%, respectively (Table 1). Olivine has a corroded rim and is surrounded by a corona consisting of fine-to-medium sized (<0.05 and 0.05–2 mm), euhedral-to-subhedral clinopyroxene (Fig. 5A, B and C). The clinopyroxene composition (Table 1) varies from diopside (Mg# = 88–98, coloured light green in Fig. 5B) to augite (Mg#≈78, dark green in Fig. 4C). Surrounding the clinopyroxene corona there is a randomly oriented subhedral mica corona (Fig. 5A, B and C). This mica (Mg# = 83–85) is phlogopite (0.05–2 mm) with (wt%): 1.3–6.1 TiO_2; 0.1–0.4 BaO; 1–1.5 F; with 2.4–3.7 H_2O (Table 3). Clinopyroxene and phlogopite host randomly distributed (primary) melt inclusions (up to 20 μm, Fig. 5D) and mineral inclusions (<50 μm) of magnetite and perovskite. Fine-to-medium grained (<0.05–2 mm) ilmenite, diopside, and zirconolite form a symplectic microtexture in both parts of the double corona (Fig. 5E and F, Tables 1 and 2). Glass is not present in the xenolith investigated.

4.2. Host nephelinite enclosing the olivine-phlogopite micro-ijolite

The volcanic rock encasing the micro-ijolite is fine-to-medium-grained (<0.05–2 mm) nephelinite. It consists of clinopyroxene, nepheline, garnet, and wollastonite phenocrysts together with a glassy greenish-to-brownish groundmass (Fig. 6A). The glass has moderate SiO_2 content (all in wt%) (46.3–51.2), high Na_2O + K_2O content (11.4–20.0), and high FeO^T content (4.5–20.1), while MgO content is low (0.7–1.2). It is strongly peralkaline [molar $(Na_2O + K_2O)/Al_2O_3$ = 2.8–5.7] (Table 4) and contains rounded (up to 200 μm in size) post-magmatic carbonate-filled vesicles (Fig. 6A–D).

The clinopyroxene (Fig. 6B and E) has an overall aegirine-augite composition with (all in wt%) 14.4–21.3 FeO^T, 1.5–3.2 Na_2O, and 5.5–9.7 MgO (Table 4). The clinopyroxene encloses garnet and nepheline inclusions (<100 μm). The nepheline phenocrysts are euhedral

Table 2
Representative composition (wt%) of magnetite, perovskite, ilmenite and zirconolite from the olivine-phlogopite micro-ijolite, Oldoinyo Lengai, Tanzania. EDS: Energy Dispersive Spectrometry.

	Ijolite																			
	magnetite (WDS)								**perovskite (WDS)**				**symplectite**							
	magnetite inclusion								***perovskite inclusion***				***ilmenite (EDS)***				***zirconolite (EDS)***			
	in titanite		*in double corona*		*in matrix diopside*		*in phlogopite phenocryst*		*in matrix diopside*		*in phlogopite phenocryst*									
SiO_2	b.d.	b.d.	b.d.	b.d.	b.d.	b.d.	b.d.	b.d.	0.08	0.01	0.71	0.96	1.09	0.76	0.83	0.89	b.d.	b.d.	b.d.	b.d.
TiO_2	11.25	11.29	11.87	11.33	7.87	10.05	8.07	9.07	54.47	53.34	55.27	55.92	50.33	50.58	50.46	50.71	37.51	36.26	35.36	33.88
Al_2O_3	0.27	0.32	0.06	0.05	0.30	0.27	0.65	0.33	b.d.	b.d.	b.d.	b.d.	0.13	0.12	0.31	0.22	b.d.	b.d.	b.d.	b.d.
FeO^T	84.83	85.45	82.93	82.33	86.83	86.28	88.23	87.44	1.16	1.15	1.61	0.71	40.17	40.21	40.89	39.94	6.50	6.71	6.63	6.71
Cr_2O_3	0.12	0.15	0.25	0.20	0.30	0.25	0.31	0.29	b.d.	b.d.	b.d.	b.d.	b.d.	b.d.	b.d.	b.d.	b.d.	b.d.	b.d.	b.d.
MnO	0.63	0.71	0.62	0.52	0.54	0.59	0.60	0.53	b.d.	b.d.	b.d.	b.d.	2.01	1.88	1.71	1.80	b.d.	b.d.	b.d.	b.d.
MgO	1.67	1.29	3.32	3.38	0.68	0.56	1.16	0.65	b.d.	b.d.	b.d.	b.d.	5.86	6.21	5.67	6.05	b.d.	b.d.	b.d.	b.d.
CaO	b.d.	b.d.	b.d.	b.d.	b.d.	b.d.	b.d.	b.d.	38.46	38.80	37.32	37.66	0.17	0.23	0.14	0.40	13.29	12.01	12.02	11.56
Na_2O	b.d.	b.d.	b.d.	b.d.	b.d.	b.d.	b.d.	b.d.	0.52	0.29	0.50	0.51	b.d.	b.d.	b.d.	b.d.	0.21	0.39	0.36	0.39
La_2O_3	b.d.	b.d.	b.d.	b.d.	b.d.	b.d.	b.d.	b.d.	0.23	0.20	b.d.	b.d.	b.d.	b.d.	b.d.	b.d.	b.d.	b.d.	0.02	0.42
Nb_2O_5	b.d.	b.d.	b.d.	b.d.	b.d.	b.d.	b.d.	b.d.	0.28	0.21	0.59	b.d.	b.d.	b.d.	b.d.	b.d.	4.39	4.25	4.49	4.89
Ce_2O_3	b.d.	b.d.	b.d.	b.d.	b.d.	b.d.	b.d.	b.d.	0.44	0.60	b.d.	b.d.	b.d.	b.d.	b.d.	b.d.	2.09	2.10	1.85	2.20
UO_2	b.d.	b.d.	b.d.	b.d.	b.d.	b.d.	b.d.	b.d.	b.d.	0.05	0.01	0.16	b.d.	b.d.	b.d.	b.d.	1.32	0.86	1.40	1.49
ThO_2	b.d.	b.d.	b.d.	b.d.	b.d.	b.d.	b.d.	b.d.	0.05	0.06	0.24	0.03	b.d.	b.d.	b.d.	b.d.	1.68	1.86	2.13	2.46
ZrO_2	b.d.	b.d.	b.d.	b.d.	b.d.	b.d.	b.d.	b.d.	b.d.	b.d.	b.d.	b.d.	b.d.	b.d.	b.d.	b.d.	28.07	30.03	31.96	31.48
Total	98.76	99.19	99.05	97.81	96.52	97.99	99.03	98.31	95.69	94.71	96.25	95.94	99.76	99.99	100.01	100.01	95.06	94.47	96.22	95.48
formula based on: 3 cations and 4 oxygens									2 cations and 3 oxygens				2 cations and 4 oxygens				4 cations and 7 oxygens			
Si	–	–	–	–	–	–	–	–	0.000	0.000	0.020	0.020	0.027	0.019	0.020	0.022	–	–	–	–
Ti^{IV}	0.306	0.307	0.319	0.308	0.220	0.278	0.220	0.250	0.980	0.970	0.980	0.980	0.928	0.932	0.931	0.932	1.734	1.694	1.639	1.598
Al	0.011	0.014	0.002	0.002	0.013	0.012	0.028	0.014	–	–	–	–	0.004	0.003	0.009	0.006	–	–	–	–
Fe^{II}	1.199	1.216	1.124	1.110	1.166	1.231	1.139	1.198	0.000	0.000	0.000	0.000	0.824	0.823	0.839	0.816	0.000	0.000	0.000	0.000
Fe^{III}	1.371	1.368	1.353	1.377	1.537	1.424	1.533	1.478	–	–	–	–	0.000	0.000	0.000	0.000	0.334	0.348	0.341	0.352
Cr	0.003	0.004	0.007	0.006	0.009	0.007	0.008	0.008	–	–	–	–	0.000	0.000	0.000	0.000	–	–	–	–
Mn	0.019	0.021	0.019	0.016	0.017	0.018	0.018	0.016	–	–	–	–	0.041	0.038	0.035	0.037	–	–	–	–
Mg	0.090	0.069	0.177	0.182	0.038	0.031	0.063	0.036	–	–	–	–	0.214	0.227	0.207	0.220	–	–	–	–
Ca	–	–	–	–	–	–	–	–	0.990	1.010	0.950	0.950	0.004	0.006	0.004	0.010	0.875	0.799	0.793	0.777
Na	–	–	–	–	–	–	–	–	0.020	0.010	0.020	0.020	–	–	–	–	0.025	0.047	0.043	0.047
La	–	–	–	–	–	–	–	–	0.000	0.000	0.000	0.000	–	–	–	–	–	–	0.000	0.010
Nb	–	–	–	–	–	–	–	–	0.000	0.000	0.010	0.000	–	–	–	–	0.122	0.119	0.125	0.139
Ce	–	–	–	–	–	–	–	–	0.000	0.100	–	–	–	–	–	–	0.047	0.048	0.042	0.051
U	–	–	–	–	–	–	–	–	0.000	0.000	0.000	0.000	–	–	–	–	0.018	0.012	0.019	0.021
Th	–	–	–	–	–	–	–	–	0.000	0.000	0.000	0.000	–	–	–	–	0.024	0.026	0.030	0.035
Zr	–	–	–	–	–	–	–	–	–	–	–	–	–	–	–	–	0.842	0.910	0.961	0.963
Sum	3.001	3.000	3.000	3.000	3.000	3.001	3.008	3.000	1.990	2.090	1.980	1.970	2.043	2.048	2.045	2.043	4.021	4.004	3.994	3.992

Table 3
Representative composition (wt%) of mica, titanite and nepheline from the olivine-phlogopite micro-ijolite, Oldoinyo Lengai, Tanzania.

	Ijolite																						
	mica (WDS)											**titanite (WDS)**								**nepheline (WDS)**			
	double corona			***ijolite matrix***								***ijolite matrix***								***ijolite matrix***			
	phlogopite in double corona			*phlogopite phenocryst*				*biotite rim*				*subhedral*				*anhedral*							
SiO_2	38.11	41.39	39.34	37.74	37.87	38.23	37.69	37.49	37.55	37.66	36.73	29.43	28.75	28.24	29.36	29.90	28.03	28.67	28.55	40.59	40.70	40.61	40.73
TiO_2	6.12	1.31	3.96	5.38	4.70	4.77	4.95	4.04	4.37	4.43	4.63	37.62	37.02	36.58	37.56	37.91	36.61	36.88	37.81	b.d.	b.d.	b.d.	b.d.
Al_2O_3	14.52	9.08	11.85	14.39	14.35	14.39	14.53	11.41	11.37	10.94	13.17	0.31	0.33	0.35	0.33	0.35	0.36	0.36	0.36	32.59	32.83	32.56	32.19
FeO^T	7.27	8.41	7.35	7.53	8.04	6.53	8.32	18.80	18.93	19.10	16.27	1.72	2.00	2.13	1.87	1.60	2.08	1.84	2.19	1.70	1.93	2.04	1.76
Cr_2O_3	b.d.	b.d.	b.d.	b.d.	b.d.	b.d.	b.d.	b.d.	b.d.	b.d.	b.d.	b.d.	b.d.	b.d.	b.d.	b.d.	b.d.	b.d.	b.d.	b.d.	b.d.	b.d.	b.d.
MnO	0.06	0.12	0.09	0.07	0.06	0.05	0.02	0.38	0.37	0.32	0.32	b.d.	b.d.	b.d.	b.d.	b.d.	b.d.	b.d.	b.d.	b.d.	b.d.	b.d.	b.d.
MgO	20.50	24.25	22.63	20.33	20.08	20.49	19.87	13.96	13.81	13.31	14.38	b.d.	b.d.	b.d.	b.d.	b.d.	b.d.	b.d.	b.d.	b.d.	b.d.	b.d.	b.d.
SrO	b.d.	b.d.	b.d.	b.d.	b.d.	b.d.	b.d.	b.d.	b.d.	b.d.	b.d.	b.d.	b.d.	b.d.	b.d.	b.d.	b.d.	b.d.	b.d.	b.d.	b.d.	b.d.	b.d.
CaO	b.d.	b.d.	b.d.	b.d.	b.d.	b.d.	b.d.	b.d.	b.d.	b.d.	b.d.	27.52	27.48	27.07	27.67	27.47	27.50	27.64	27.35	0.09	0.09	0.10	0.09
Na_2O	0.42	0.40	0.39	0.41	0.34	0.36	0.43	0.43	0.37	0.45	0.39	0.21	0.17	0.17	0.11	0.15	0.14	0.16	0.18	16.36	16.24	16.24	16.21
K_2O	9.48	9.82	9.71	9.63	9.70	9.62	9.67	9.08	9.24	9.12	9.28	b.d.	b.d.	b.d.	b.d.	b.d.	b.d.	b.d.	b.d.	6.13	6.52	6.37	6.34
BaO	0.14	0.05	0.36	0.14	0.20	0.14	0.22	0.19	0.20	0.22	0.07	b.d.	b.d.	b.d.	b.d.	b.d.	b.d.	b.d.	b.d.	b.d.	b.d.	b.d.	b.d.
F	0.95	1.49	1.16	0.96	0.92	0.98	0.89	0.62	0.62	0.67	0.58	b.d.	b.d.	b.d.	b.d.	b.d.	b.d.	b.d.	b.d.	b.d.	b.d.	b.d.	b.d.
Cl	0.02	b.d.	b.d.	0.02	0.01	0.01	0.02	0.02	b.d.	0.02	0.01	b.d.	b.d.	b.d.	b.d.	b.d.	b.d.	b.d.	b.d.	b.d.	b.d.	b.d.	b.d.
Zr	b.d.	b.d.	b.d.	b.d.	b.d.	b.d.	b.d.	b.d.	b.d.	b.d.	b.d.	0.35	0.08	0.15	0.47	0.40	0.10	0.12	0.50	b.d.	b.d.	b.d.	b.d.
La	b.d.	b.d.	b.d.	b.d.	b.d.	b.d.	b.d.	b.d.	b.d.	b.d.	b.d.	0.10	0.01	0.08	0.02	b.d.	b.d.	b.d.	b.d.	b.d.	b.d.	b.d.	b.d.
Nb	b.d.	b.d.	b.d.	b.d.	b.d.	b.d.	b.d.	b.d.	b.d.	b.d.	b.d.	0.27	0.14	0.37	0.29	0.13	0.14	0.20	0.19	b.d.	b.d.	b.d.	b.d.
Ce	b.d.	b.d.	b.d.	b.d.	b.d.	b.d.	b.d.	b.d.	b.d.	b.d.	b.d.	b.d.	0.01	0.22	b.d.	0.02	0.06	b.d.	b.d.	b.d.	b.d.	b.d.	b.d.
U	b.d.	b.d.	b.d.	b.d.	b.d.	b.d.	b.d.	b.d.	b.d.	b.d.	b.d.	b.d.	b.d.	0.05	b.d.	b.d.	b.d.	b.d.	0.01	b.d.	b.d.	b.d.	b.d.
Th	b.d.	b.d.	b.d.	b.d.	b.d.	b.d.	b.d.	b.d.	b.d.	b.d.	b.d.	0.01	0.02	b.d.	0.04	0.02	b.d.	0.01	b.d.	b.d.	b.d.	b.d.	b.d.
Total	97.60	96.32	96.85	96.60	96.27	95.57	96.60	96.41	96.83	96.24	95.83	97.55	96.01	95.42	97.71	97.95	95.00	95.87	97.13	97.45	98.32	97.91	97.32
formula based on: 8 cations 11 oxygens												3 cations and 5 oxygens								12 cations and 16 oxygens			
Si	2.717	3.020	2.842	2.726	2.750	2.773	2.731	2.856	2.852	2.882	2.780	1.013	0.989	0.972	1.010	1.029	0.964	0.986	0.982	4.056	4.043	4.051	4.080
Ti	0.328	0.072	0.215	0.292	0.257	0.260	0.270	0.232	0.250	0.255	0.264	0.974	0.958	0.947	0.972	0.981	0.948	0.955	0.979	–	–	–	–
Al	1.220	0.781	1.009	1.225	1.228	1.230	1.241	1.025	1.018	0.987	1.175	0.013	0.013	0.014	0.013	0.014	0.015	0.014	0.014	3.838	3.844	3.828	3.802
Fe	–	–	–	–	–	–	–	–	–	–	–	0.050	0.058	0.061	0.054	0.046	0.060	0.053	0.063	0.142	0.160	0.170	0.148
Fe^{II}	0.433	0.513	0.444	0.455	0.488	0.396	0.504	1.198	1.202	1.222	1.030	–	–	–	–	–	–	–	–	–	–	–	–
Fe^{III}	–	–	–	–	–	–	–	–	–	–	–	–	–	–	–	–	–	–	–	–	–	–	–
Mn	0.004	0.007	0.005	0.004	0.004	0.000	0.001	0.024	0.023	0.020	0.020	–	–	–	–	–	–	–	–	–	–	–	–
Mg	2.179	2.638	2.437	2.189	2.174	2.216	2.147	1.586	1.564	1.518	1.622	–	–	–	–	–	–	–	–	–	–	–	–
Ca	–	–	–	–	–	–	–	–	–	–	–	1.015	1.013	0.998	1.020	1.013	1.014	1.019	1.008	0.009	0.010	0.011	0.010
Na	0.058	0.057	0.055	0.057	0.048	0.051	0.060	0.064	0.054	0.067	0.057	0.014	0.012	0.011	0.007	0.010	0.009	0.011	0.012	3.169	3.127	3.141	3.148
K	0.862	0.914	0.895	0.888	0.899	0.890	0.894	0.883	0.895	0.890	0.896	–	–	–	–	–	–	–	–	0.78	0.827	0.810	0.84
Ba	0.004	0.001	0.010	0.004	0.006	0.000	0.006	0.006	0.006	0.007	0.002	–	–	–	–	–	–	–	–	–	–	–	–
Zr	–	–	–	–	–	–	–	–	–	–	–	0.006	0.001	0.003	0.008	0.007	0.002	0.002	0.008	–	–	–	–
La	–	–	–	–	–	–	–	–	–	–	–	0.001	0.000	0.001	–	–	–	–	–	–	–	–	–
Nb	–	–	–	–	–	–	–	–	–	–	–	0.004	0.002	0.006	0.004	0.002	0.002	0.003	0.003	–	–	–	–
Ce	–	–	–	–	–	–	–	–	–	–	–	0.000	0.000	0.003	0.000	0.000	0.001	0.000	0.000	–	–	–	–
U	–	–	–	–	–	–	–	–	–	–	–	–	–	0.000	–	–	–	–	0.000	–	–	–	–
Th	–	–	–	–	–	–	–	–	–	–	–	0.000	0.000	–	0.000	0.000	–	0.000	–	–	–	–	–
Sum	7.805	8.003	7.913	7.841	7.853	7.816	7.856	7.873	7.865	7.849	7.846	3.089	3.047	3.016	3.090	3.102	3.014	3.043	3.070	11.996	12.011	12.011	12.031
mg#	83	84	85	83	82	85	81	57	57	55	61												

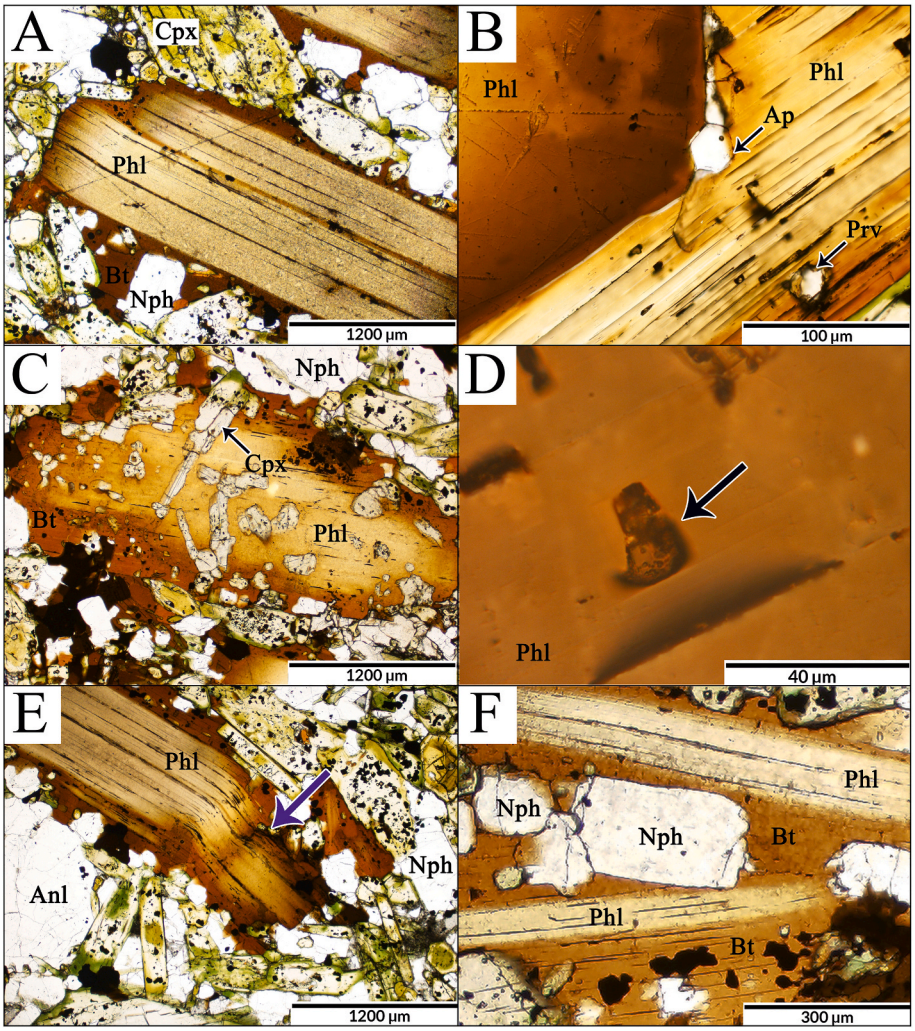

Fig. 4. Petrographic images of mica phenocrysts in the olivine-phlogopite micro-ijolite xenolith, Oldoinyo Lengai, Tanzania. (A) phenocryst with phlogopite core and biotite rim; (B) phlogopite hosting apatite and perovskite inclusions; (C) diopside inclusions; (D) primary melt inclusion shown by black arrow; (E) mica shows ductile deformation (purple arrow); (F) biotite rim enclosing groundmass minerals. Abbreviations (Whitney and Evans, 2010): Phl – phlogopite, Ap – apatite, Nph – nepheline, Prv – perovskite, Anl – analcime, Cpx – clinopyroxene.

(Fig. 6A, C and E) and homogeneous in composition (Table 4), with slightly higher FeO^T contents (1.2–4.6 wt%) than those in the micro-ijolite. Nepheline encloses acicular clinopyroxene mineral inclusions (Fig. 6C). Garnet occurs as euhedral, reddish-brown-to-black phenocrysts (Fig. 6B and D). It is rich (all in wt%) in TiO_2 (10.8–17.1), CaO (32.1–32.5), and FeO^T (20.4–23.3) (Table 4). On the basis of the classification scheme of Grew et al. (2013) for garnets with $TiO_2 > 12$ wt%, the garnet is identified as a solid solution of Ti-rich andradite and schorlomite. The garnet contains nepheline and clinopyroxene (Fig. 6D) mineral inclusions. Wollastonite is homogeneous (Table 4) and occurs as both euhedral and subhedral crystals without mineral inclusions (Fig. 6A and E). The nephelinite also contains magnetite (Fig. 6F).

5. Discussion

5.1. Estimation of the formation conditions

The coexistence of titanite, perovskite, nepheline, and clinopyroxene (Fig. 3) allowed us to estimate the formation conditions of the olivine-phlogopite micro-ijolite groundmass, based on the stability of these minerals as a function of SiO_2 activity and temperature (Carmichael et al., 1970). Fig. 7 shows the reaction curves of perovskite-titanite and nepheline-albite intersecting at 1040 °C. As albite is not present in our sample, this temperature is considered to be the maximum crystallization temperature for the olivine-phlogopite micro-ijolite groundmass under plutonic conditions.

5.1.1. Clinopyroxene crystallization conditions

To determine the formation temperature of the groundmass, we used the clinopyroxene thermometer of Putirka (1996, 2008), which is based on pyroxene-silicate melt equilibrium. Due to the lack of melt phase data in this study, we paired the compositions of our diopside and aegirine-augite zones (Fig. 3 and Tables 1 and 5) with published melt composition data from similar systems (Berkesi et al., 2020; Guzmics et al., 2012, Table 5). The applied silicate melt compositions are from melt inclusions (Kerimasi and Oldoinyo Lengai) hosted in: (1) perovskite coexisting with diopside (Guzmics et al., 2012) (see as melt-1 in Table 5); and (2) nepheline in co-precipitation with aegirine-augite (Berkesi et al., 2020) (see as melt-2 in Table 5). Our calculations for diopside–melt-1 and aegirine-augite–melt-2 pairs suggest equilibrium temperatures of 970–1070 °C and 830–960 °C, respectively (Table 5). The data calculated for diopside is consistent with homogenization temperatures observed in diopside-bearing rocks (~1050 °C, Guzmics et al., 2012). Temperature data for aegirine-augite appear to be overestimated when compared to homogenization temperatures in aegirine-augite–bearing rocks (750–850 °C, Berkesi et al., 2020; Guzmics et al., 2019), even if we consider the precision of the thermometer (±27 °C). Fig. 3C shows that only the diopside zones contain perovskite inclusions. This is consistent with the data of Fig. 7, showing that at constant SiO_2 activity perovskite becomes stable with increasing temperature rather than titanite. Accordingly, aegirine-augite, formed at lower temperature than diopside, coexists with titanite (Fig. 3D).

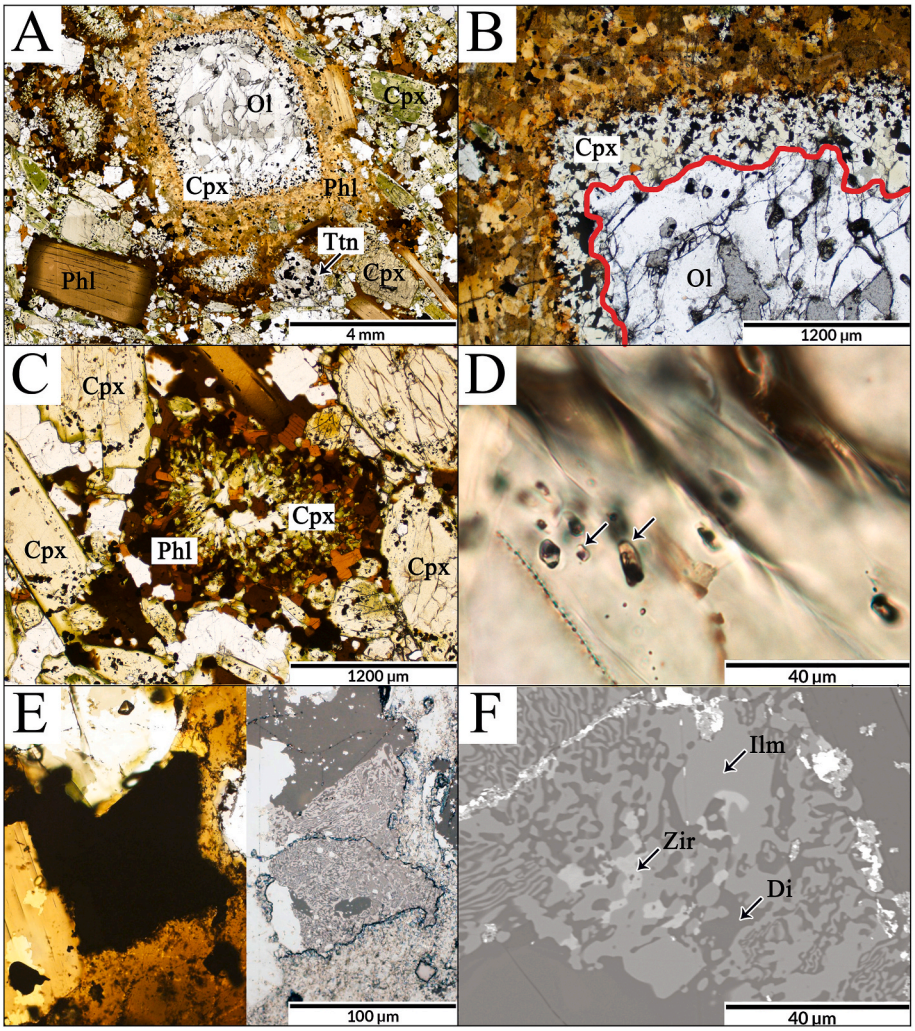

Fig. 5. Petrographic images (A–E) and back-scattered electron images (E–F): (A) olivine surrounded by a double corona and groundmass; (B) olivine surrounded by the double corona, the contact of olivine and clinopyroxene shown with the red line; (C) double corona lacking olivine and with dark green clinopyroxene; (D) primary melt inclusions in clinopyroxene indicated with arrows; (E) symplectic microtexture in the double corona in plane polarized light and in a back-scattered electron image; (F) symplectic microtexture in the double coronas. Abbreviations (Whitney and Evans, 2010): Cpx – clinopyroxene, Phl – phlogopite, Ol – olivine, Ilm – ilmenite, Zir – zirconolite, Di – diopside, Ttn – titanite.

5.1.2. Titanite crystallization conditions

To test independently the crystallization temperatures of aegirine-augite-titanite, the Zr-in-titanite thermometer of Hayden et al. (2007) was used. To apply this approach, the crystallization pressure and SiO_2 and TiO_2 activities of the system must also be estimated using the Zr content of the titanite. On the basis of the log$aSiO_2$ temperature diagram of Carmichael et al. (1970) (Fig. 7) and considering that aegirine-augite crystals usually contain titanite inclusions, $aSiO_2$ can be estimated to be ~0.05 during their co-precipitation. In the absence of rutile in the paragenesis, $aTiO_2 = 0.5$ was chosen, as suggested by Hayden et al. (2007), with 0.4–0.6 GPa pressure, and as a result 700–780 °C could be calculated as crystallization temperatures for titanite. The thermometer gives the most accurate values between 600 and 1000 °C, with ±20 °C, so the results of this thermometer could be trusted. Moreover, in their original article; Hayden et al. (2007) used titanites with Zr-contetnt of 577–5459 ppm whereas our titanites have Zr-content of 760–4990 ppm, further supporting the veracity of the geothermometer.

The result of 700–780 °C is consistent with the homogenization temperatures of melt inclusions (750–850 °C) from aegirine-augite and titanite-bearing rocks (Berkesi et al., 2020; Guzmics et al., 2019) rather than with our calculated data from aegirine-augite melt thermometry. For this reason, we have used the homogenization temperature data for clinopyroxene in our evolutionary model below.

5.1.3. Mica crystallization and re-equilibration conditions

For the mica occurring in the olivine-phlogopite micro-ijolite, the Ti-in-mica geothermometer of Henry et al. (2005) was used. This thermometer was originally calibrated for metapelites but has also been successfully used for magmatic systems and for determining magmatic-hydrothermal temperatures in porphyry copper systems (Babazadeh et al., 2019; Rezaei and Zarasvandi, 2019). The accuracy of the thermometer is ±12–24 °C. This precision might be less case when it is not used for ilmenite- and rutile-bearing peraluminous metapelites. The method is based on the observation that the incorporation of Ti into mica is a temperature-dependent process. The presence of Ti-bearing minerals (perovskite, titanite and magnetite, Fig. 3) coexisting with the mica is important because without these the calculated temperature would only be a minimum temperature. Using the Ti-in-mica geothermometer for the phlogopite cores of phenocrysts (Fig. 4), a temperature range of between 700 and 800 °C (later referred to as ~750 °C) was calculated (Fig. 8). However, experimentally determined phase equilibria in SiO_2-undersaturated mafic systems show higher formation temperatures (>900 °C) for phlogopites (Speer, 1984, Veksler et al., 1998a; b). Therefore, our phlogopite phenocryst data (Fig. 8) suggest post-magmatic re-equilibration at lower temperatures. The initial Ti content of the phlogopite phenocrysts might have been altered by Ti exchange with the surrounding Ti-bearing minerals (Fig. 3E and F, and 4B) as temperature decreased. The biotite rim around the phlogopite (Fig. 4A, E and F) gives lower equilibrium temperatures of 600–700 °C (later referred to as ~650 °C) (Fig. 8) than the phlogopite phenocrysts. Similar results could be calculated using the published data from phlogopite and biotite (Dawson et al., 1995; Sekisova et al., 2015) from

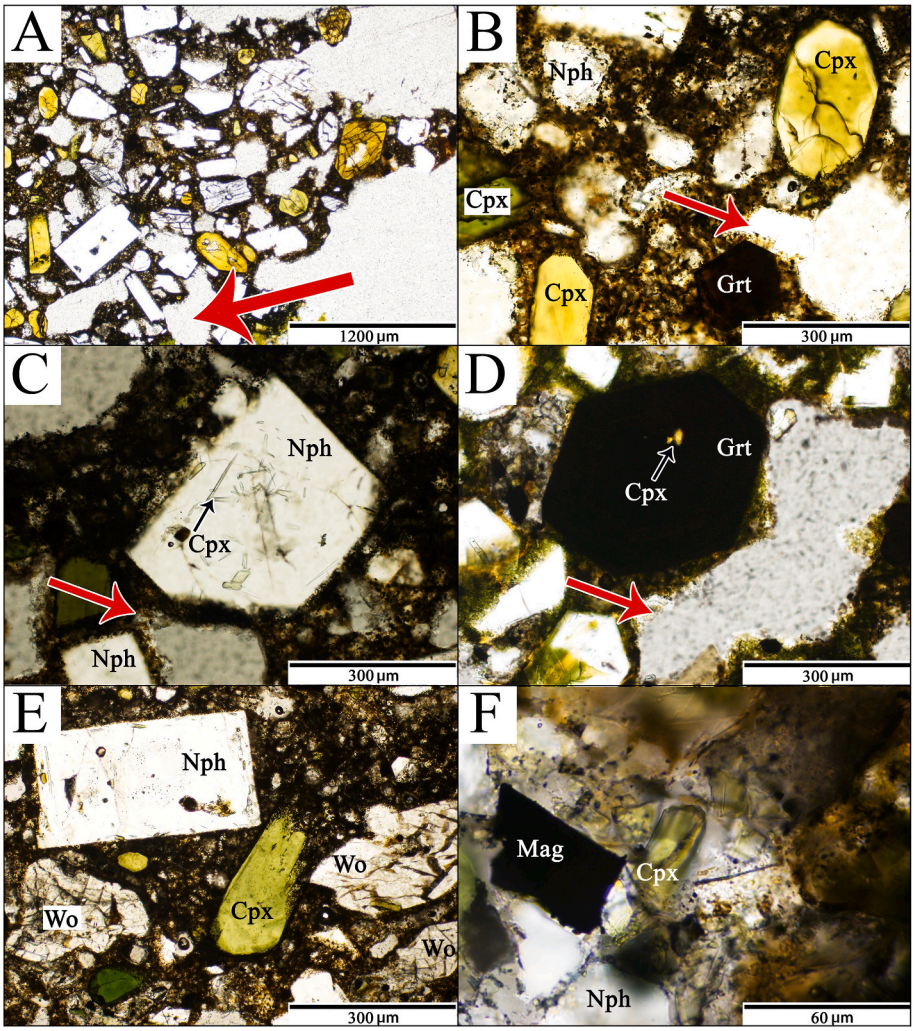

Fig. 6. Petrographic images of nephelinite, Oldoinyo Lengai, Tanzania. (A) phenocrysts of nepheline, clinopyroxene, wollastonite, garnet. Vesicles are marked with red arrow; (B) clinopyroxene and garnet phenocrysts; (C) clinopyroxene inclusion in nepheline; (D) clinopyroxene inclusion in garnet; (E) phenocrysts of nepheline, clinopyroxene and wollastonite; (F) magnetite, clinopyroxene and nepheline microphenocrysts in the glassy groundmass. Abbreviations (Whitney and Evans, 2010): Cpx – clinopyroxene, Grt – garnet, Nph – nepheline, Mag – magnetite, Wo – wollastonite.

Oldoinyo Lengai olivine-phlogopite micro-ijolites, which also contain titanite, perovskite, and magnetite (Fig. 8). We suggest that the micas are primary magmatic minerals formed above 900 °C based on literature (Speer, 1984, Veksler et al., 1998a; b), however, with the thermometer we could find two post-magmatic re-equilibration temperatures: one for phlogopite phenocrysts (~750 °C) and one for the biotite rim (~650 °C). In contrast to the phlogopite phenocrysts, the geothermometer for the phlogopite of the double corona gives an unrealistically wide temperature range of 500–800 °C (Fig. 8). This is possible, as chemical equilibrium with the surrounding Ti-bearing minerals (e.g., titanite, perovskite and magnetite) was not attained. A similarly wide temperature range could be calculated for the compositions of corona phlogopites reported by Dawson et al. (1995) from Oldoinyo Lengai (Fig. 8).

5.1.3.1. Depth calculation. Using an equilibrium temperature of 750 °C (phlogopite phenocryst) and assuming a geothermal gradient of ~40–65 °C/km (Nyblade, 1997), we estimated a depth of 10–20 km for the above-determined re-equilibration of phlogopite phenocrysts.

5.2. Evolution of olivine-phlogopite micro-ijolites

The evolution of the olivine-phlogopite micro-ijolites proposed here is based on our data and that of Dawson and Smith (1992), Dawson et al. (1995) and Sekisova et al. (2015). Fig. 9 shows theoretical evolutionary steps, including the proposed existence of three magma chambers (M.C. 1, 2, 2/2) (Fig. 9A), involved in the formation of the olivine-phlogopite micro-ijolites.

5.2.1. Formation of olivine in magma chamber 1 (M.C. 1)

Fig. 10 shows that olivines from Oldoinyo Lengai olivine-phlogopite micro-ijolites (this study; Dawson and Smith, 1992a; Dawson et al., 1995; Sekisova et al., 2015) have lower Mg# (79–84) and higher Ca (1280–2500 ppm) than olivines derived from lithospheric mantle sources (Mg# $\geq$ 90 and Ca $<$ 1000 ppm). The difference in Mg# and Ca-content is also significant when comparing the composition of kimberlite-, and ijolite-hosted olivines (McDonough and Rudnick, 1998; Simkin and Smith, 1970). Even though olivines in kimberlites have lower Mg# and higher Ca than lithospheric mantle olivines (Giuliani, 2018; Nowicki et al., 2008; Scott Smith et al., 2013), in this study olivine have higher Ca-contents than those typical of kimberlites.

In contrast to the widely accepted model of a mantle origin for the olivines in micro-ijolites (Dawson and Smith, 1988, 1992a; Dawson et al., 1995; Sekisova et al., 2015), we support the idea that olivine is an early magmatic liquidus phase from a silicate melt of metasomatized mantle origin (Keller et al., 2006; Giuliani, 2018; Baudouin and Parat, 2020). The silicate melt that formed olivine could have been a carbonated olivine-nephelinite melt formed by partial melting of a CO_2-bearing and metasomatized mantle at $\leq$ 3 GPa (Brey, 1978; Green et al., 1987; Green, 2015). Olivine nephelinite has also been proposed as parent melt of the Oldoinyo Lengai suite (Peterson and Kjarsgaard, 1995; Dawson, 1998; Keller et al., 2006; Klaudius and Keller, 2006). Therefore, the olivine should be considered as antecrysts which crystallized and grew

Table 4
Representative composition (wt%) of nepheline, clinopyroxene, garnet, wollastonite and glass from the nephelinite, Oldoinyo Lengai, Tanzania.

	Nephelinite																			
	groundmass phases (WDS)																			
	nepheline				glass				clinopyroxene				garnet				wollastonite			
									aegirine-augite				*schorlomite-melanite solid solution*							
SiO_2	40.47	40.22	41.11	40.82	46.98	46.32	48.77	48.96	51.05	51.29	51.47	49.85	29.32	28.82	29.35	27.82	51.35	50.73	51.01	52.02
TiO_2	b.d.	b.d.	b.d.	b.d.	3.01	2.99	0.92	0.79	0.31	0.40	0.72	0.51	12.24	13.75	16.59	14.61	0.07	0.06	0.05	0.23
Al_2O_3	32.36	32.64	32.81	32.00	3.47	3.03	4.50	5.76	0.60	0.64	1.00	0.98	0.73	0.92	1.35	0.75	0.12	0.07	0.12	0.08
FeO^T	1.42	1.23	1.41	2.10	19.06	20.19	4.54	5.18	19.09	16.11	8.17	20.57	23.27	21.92	19.72	21.70	0.98	1.10	1.03	0.76
Cr_2O_3	b.d.	b.d.	b.d.	b.d.	b.d.	b.d.	b.d.	b.d.	b.d.	0.000	0.03	0.02	b.d.	b.d.	b.d.	0.01	b.d.	b.d.	b.d.	b.d.
MnO	b.d.	b.d.	b.d.	b.d.	0.70	0.74	0.63	0.62	0.45	0.24	0.12	0.34	0.20	0.21	0.40	0.15	0.16	0.46	0.40	0.40
MgO	b.d.	b.d.	b.d.	b.d.	1.08	0.82	0.71	0.82	6.48	8.52	13.65	5.86	0.50	0.55	1.12	0.75	0.18	0.19	0.24	0.02
SrO	b.d.	b.d.	b.d.	b.d.	0.67	0.65	0.29	0.37	b.d.	0.04	0.03	0.04	0.04	0.01	0.08	0.03	0.24	0.09	0.29	0.01
CaO	b.d.	b.d.	b.d.	b.d.	3.60	1.70	16.53	14.83	18.17	20.81	24.09	18.76	32.39	32.37	30.99	32.16	45.68	45.36	45.02	46.08
Na_2O	16.06	15.61	15.83	16.15	7.93	10.33	18.49	17.56	3.14	2.03	0.75	2.84	0.24	0.42	0.41	0.27	0.22	0.24	0.15	0.33
K_2O	6.47	6.80	6.86	6.32	7.05	7.04	1.89	2.42	b.d.	b.d.	b.d.	b.d.	b.d.	b.d.	b.d.	b.d.	b.d.	b.d.	b.d.	b.d.
BaO	b.d.	b.d.	b.d.	b.d.	0.73	0.65	0.11	0.04	b.d.	b.d.	b.d.	b.d.	b.d.	b.d.	b.d.	b.d.	b.d.	b.d.	b.d.	b.d.
SO_3	b.d.	b.d.	b.d.	b.d.	2.73	3.34	0.15	0.06	b.d.	b.d.	b.d.	b.d.	b.d.	b.d.	b.d.	b.d.	b.d.	b.d.	b.d.	b.d.
P_2O_5	b.d.	b.d.	b.d.	b.d.	0.50	0.35	0.61	0.82	b.d.	b.d.	b.d.	b.d.	b.d.	b.d.	b.d.	b.d.	b.d.	b.d.	b.d.	b.d.
F	b.d.	b.d.	b.d.	b.d.	1.15	0.91	0.13	0.14	b.d.	b.d.	b.d.	b.d.	b.d.	b.d.	b.d.	b.d.	b.d.	b.d.	b.d.	b.d.
Cl	b.d.	b.d.	b.d.	b.d.	0.94	0.87	0.06	0.03	b.d.	b.d.	b.d.	b.d.	b.d.	b.d.	b.d.	b.d.	b.d.	b.d.	b.d.	b.d.
Total	96.79	96.49	98.02	97.39	99.60	99.90	98.35	98.38	99.29	100.08	100.01	99.77	98.93	98.95	100.01	98.23	99.00	98.29	98.30	99.93
	formula based on: 12 cations and 16 oxygens								4 cations and 6 oxygens				8 cations and 12 oxygens				2 cations and 3 oxygens			
Si	4.070	4.055	4.082	4.090	–	–	–	–	1.972	1.954	1.911	1.931	2.470	2.365	2.450	2.365	1.003	1.000	1.004	1.005
Ti	–	–	–	–	–	–	–	–	0.009	0.011	0.020	0.015	0.775	0.934	1.040	0.934	0.001	0.001	0.001	0.003
Al	3.837	3.879	3.840	3.780	–	–	–	–	–	–	–	–	0.073	0.075	0.130	0.075	0.003	0.002	0.003	0.002
Al^{IV}	–	–	–	–	–	–	–	–	0.019	0.029	0.044	0.045	–	–	–	–	–	–	–	–
Al^{VI}	–	–	–	–	–	–	–	–	0.008	–	–	–	–	–	–	–	–	–	–	–
Fe	0.119	0.104	0.117	0.176	–	–	–	–	–	–	–	–	–	–	–	–	0.016	0.018	0.017	0.012
Fe^{II}	–	–	–	–	–	–	–	–	0.370	0.324	0.107	0.389	0.163	0.174	0.420	0.174	–	–	–	–
Fe^{III}	–	–	–	–	–	–	–	–	0.247	0.189	0.147	0.277	1.477	1.370	0.960	1.370	–	–	–	–
Cr	–	–	–	–	–	–	–	–	–	0.000	0.001	0.001	–	–	–	0.001	–	–	–	–
Mn	–	–	–	–	–	–	–	–	0.014	0.008	0.004	0.011	0.014	0.010	0.030	0.010	0.003	0.008	0.007	0.007
Mg	–	–	–	–	–	–	–	–	0.373	0.484	0.755	0.338	0.063	0.094	0.140	0.094	0.005	0.005	0.007	0.001
Sr	–	–	–	–	–	–	–	–	–	0.001	0.001	0.001	0.002	0.001	0.000	0.001	0.003	0.001	0.003	0.000
Ca	–	–	–	–	–	–	–	–	0.752	0.849	0.958	0.779	2.924	2.930	2.770	2.930	0.956	0.958	0.950	0.954
Na	3.132	3.052	3.049	3.138	–	–	–	–	0.235	0.150	0.054	0.214	0.040	0.045	0.070	0.045	0.008	0.009	0.006	0.012
K	0.831	0.875	0.869	0.808	–	–	–	–	–	–	–	–	–	–	–	–	–	–	–	–
Sum	11.989	11.964	11.957	11.991	–	–	–	–	4.000	4.000	4.001	4.000	8.000	8.000	8.010	8.000	1.998	2.002	1.997	1.997

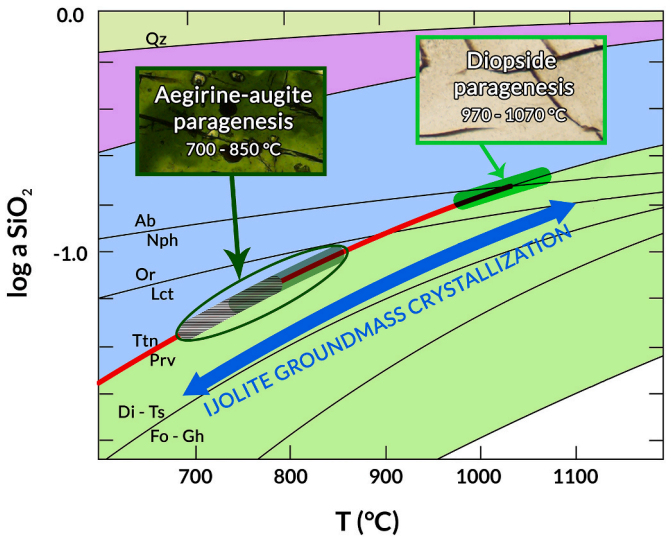

Fig. 7. Log $aSiO_2$-temperature diagram (modified from Carmichael et al., 1970), showing mineral reactions. The thick red line shows the perovskite-titanite reaction curve until 1040 °C, where it intersects with that of nepheline-albite. Because of the coexistence of nepheline-perovskite-titanite in the olivine-phlogopite micro-ijolite groundmass, 1040 °C can be considered its maximum formation temperature and the red line designates a possible crystallization path. Based on the textural evidence, homogenization temperatures of melt inclusions in similar systems, and thermometry, we could identify two regions for the groundmass crystallization: a diopside paragenesis (light green line between 970 and 1070 °C) and an aegirine-augite paragenesis with titanite (dark green circle between 700 and 850 °C). The thick grey line in the aegirine-augite paragenesis indicates the suggested titanite crystallization path, while the thick dark green line is for the aegirine-augite crystallization. Crystallization of the olivine-phlogopite micro-ijolite took place along the blue arrow. The green area is characteristic for nephelinites, blue for alkali olivine basalts, pink for tholeiites, light brown for quartz-bearing rocks. Abbreviations (Whitney and Evans, 2010): Wo – wollastonite, Fo – forsterite, Di – diopside, Gh – gehlenite, Ts – tschermak component in diopside, Prv – perovskite, Ttn – titanite, Or – orthoclase, Lct – leucite, Nph – nepheline, Ab – albite, Qz - quartz.

in the ascending nephelinite in a magma chamber (M.C. 1, Fig. 9) at crustal depths.

5.2.2. Formation of phlogopite phenocrysts (M.C. 2)

Previous interpretations of the origin of the phlogopites are controversial. One model suggests derivation from phlogopite-bearing veins (Wölbern et al., 2012), whereas others consider the phlogopite as disaggregated metasomatized mantle xenocryst/xenolith clasts (Clement, 1982; Dawson and Smith, 1992a,b; Kargin et al., 2019), or of primary magmatic origin (Baudouin and Parat, 2020). As the phlogopite phenocrysts contain primary melt inclusions and mineral inclusions of early liquidus minerals (perovskite, diopside and apatite, Fig. 4B–D), they probably crystallized from nephelinite magma in the initial phase of the olivine-phlogopite micro-ijolite formation. This hypothesis is supported by the similar compositions of perovskites that occur in both phlogopite phenocrysts (Fig. 4B, Table 2) and diopside zones in the micro-ijolite groundmass (Fig. 3C, Table 2). Numerous phlogopite phenocrysts have been co-precipitated with diopside (Fig. 4C), and the composition of these clinopyroxenes is the same as those of the diopside zones (Table 1). The above observations suggest that the phlogopite phenocrysts have a magmatic origin and that they crystallized and accumulated in M.C. 2 (Fig. 9C).

5.2.3. Olivine dissolution and formation of clinopyroxene-rich inner corona (M.C. 2)

According to our model, olivine was transferred from M.C. 1 to M.C. 2, where it was not stable, leading to its partial dissolution (shown as a corroded rim, Fig. 5B and C and 9D). Another possibility is that olivine had already crystallized in M.C. 2 and remained in place and subsequently began to dissolve partially due to an injection of nephelinite that was not in equilibrium with olivine. Dissolution features of olivine have been observed by Dawson et al. (1995) and Sekisova et al. (2015). Such olivines are usually surrounded by a clinopyroxene corona. Although a general approach for the formation of the clinopyroxene corona is as a reaction product between an olivine xenocryst and a nephelinitic magma (Dawson et al., 1995; Sekisova et al., 2015), our data do not fully support this explanation. The clinopyroxenes in the corona host randomly distributed primary melt inclusions (Fig. 5D) and they have a similar composition to the clinopyroxenes in the groundmass (Fig. 3A–C) (Table 1), clearly indicating their magmatic origin. Furthermore, olivine is known to be a potential nucleus for pyroxene in mafic melt systems. Therefore, we hypothesize that after partial dissolution of olivine antecrysts in M.C. 2, clinopyroxene with diopside composition began to crystallize on its surface (Fig. 9E).

5.2.4. Formation of phlogopite-rich outer corona (M.C. 2)

Dawson and Smith (1992b) considered that corona phlogopite in the olivine-phlogopite micro-ijolites might have originated from olivine-phlogopite pyroxenite in a manner similar to that of the phlogopite phenocrysts. These authors suggested that they are xenoliths of metasomatized peridotite from the upper mantle. The presence of melt inclusions and similar mineral inclusions (perovskite, diopside, and magnetite) in the corona phlogopites and in the ijolite groundmass does not support a mantle origin. Rather, in accordance with the results from Gardiner and Kovdor ultramafic-alkaline complexes (Nielsen et al., 1997; Veksler et al., 1998), we propose that corona phlogopites are an early and primary magmatic product associated with phlogopite phenocrysts. In our model (Fig. 9F), we suggest that the phlogopite corona on the olivine with clinopyroxene cumulate was formed due to accumulation resulting from magma dynamics and movement. There is evidence for magma movement shown by the orientation of the phlogopite phenocrysts and groundmass minerals (explained in the chapter of 4.1. And visible in Fig. 2A). We believe that magma dynamics allowed the olivine + clinopyroxene cumulate to rotate and collect crystals of phlogopite cumulates already present in M.C. 2 (Fig. 9F).

5.2.5. Formation of the ijolite groundmass (M.C. 2)

On the basis of the petrography (Fig. 3) and thermometric calculations for clinopyroxene formation (Fig. 7), two different periods are proposed for the crystallization of the groundmass. At higher temperatures (970–1070 °C), we assume the formation of diopside and nepheline with subordinate magnetite and perovskite, which we hereafter refer to as the diopside paragenesis (Figs. 7 and 9G). When the temperature decreased to 750–850 °C, the precipitation of diopside and perovskite might be replaced by aegirine-augite and titanite, which is referred to here as the aegirine-augite paragenesis (Figs. 7 and 9G).

To explain the alternate zonation of diopside and aegirine-augite (Fig. 3A and B), we propose injections of hot magmas from either M. C. 1 or another magmachamber (M.C. 2/2) filled with magma of similar composition to M.C. 2 (Fig. 9G and H), which crystallize the diopside paragenesis (970–1070 °C, Fig. 7), followed by cooling periods during which the aegirine-augite paragenesis (700–850 °C, Fig. 7) formed. Our hypothesis is supported by the presence of anhedral titanite in the groundmass (Figs. 4F and 9H). These anhedral crystals might represent resorbed titanites due to an injection of hot magma. The observed ductile deformation of the phlogopite phenocrysts (Fig. 4E), might refer to a similar hot magma injection. Our model fits well with the widely accepted model of an open plumbing system at Oldoinyo Lengai, where injection of magmas with different compositions and temperatures into a magma chamber is a common phenomenon (Dawson et al., 1995; de Moor et al., 2013; Berkesi et al., 2020; Reiss et al., 2021).

Table 5
Representative composition (wt%) of melt–diopside and melt–aegirine-augite pairs. Melt–clinopyroxene equilibrium temperature ranges were calculated based on the method of Putirka (1996, 2008). Melts data are from are from Guzmics et al. (2012) and Berkesi et al. (2020).

	Guzmics et al. (2012)	This study				
	Melt-1	Diopside zone 1	Diopside zone 2	Diopside zone 3	Diopside zone 4	Diopside zone 5
SiO_2	40.33	49.99	51.12	51.06	51.21	51.74
TiO_2	3.19	1.67	1.60	1.17	1.45	1.01
Al_2O_3	14.32	1.62	1.63	1.25	1.22	0.83
FeO^t	7.55	7.47	5.01	4.82	4.89	4.09
MnO	0.34	0.12	0.06	0.06	0.09	0.04
MgO	6.72	13.72	15.38	15.28	15.55	16.03
CaO	12.65	23.95	24.44	24.62	24.87	24.88
Na_2O	3.44	0.75	0.62	0.47	0.43	0.42
K_2O	3.14	0.00	0.00	0.00	0.00	0.00
P_2O_5	2.14	0.00	0.06	0.01	0.07	0.01
Calculated temperature (°C)		1071	1016	981	1014	973
Minimum °C	~970					
Maximum °C	~1070					
	Berkesi et al. (2020)	This study				
	Melt-2	Aegirine-augite zone 1	Aegirine-augite zone 2	Aegirine-augite zone 3	Aegirine-augite zone 4	Aegirine-augite zone 5
SiO_2	40.41	50.50	50.22	51.24	51.34	50.73
TiO_2	0.78	1.42	0.41	0.60	0.66	0.79
Al_2O_3	5.00	1.83	1.05	0.71	0.79	0.86
FeO^t	7.19	5.71	19.33	12.80	16.63	17.87
MnO	0.23	0.02	0.30	0.21	0.18	0.21
MgO	0.47	14.66	6.39	10.57	8.43	7.36
CaO	3.13	24.43	19.04	20.58	17.60	16.78
Na_2O	13.45	0.62	2.90	2.18	3.56	4.03
K_2O	5.12	0.00	0.00	0.00	0.00	0.00
P_2O_5	0.13	0.00	0.02	0.07	0.04	0.14
Calculated temperature (°C)		831	941	896	951	955
Minimum °C	~830					
Maximum °C	~960					

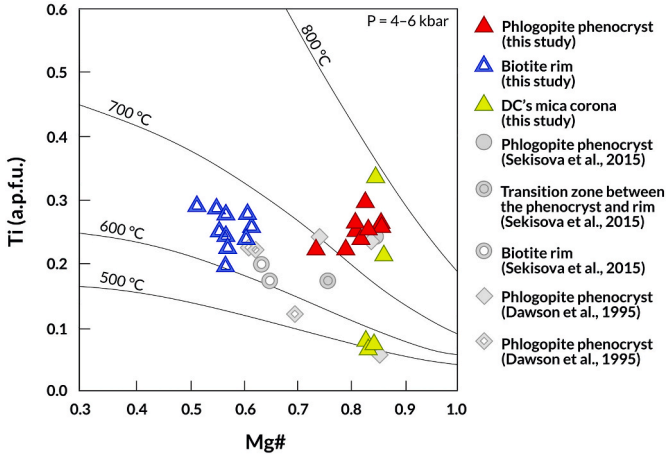

Fig. 8. Ti (a.p.f.u.) – Mg# diagram for phlogopites modified after Henry et al. (2005), showing also equilibrium temperatures calculated for phlogopite and biotite in the olivine-phlogopite micro-ijolites. We consider our data to be subsolidus rather than magmatic temperatures. For details, see the text. a. p.f.u – atom per formula unit, Mg#–MgO/(MgO + FeO), molar.

5.2.6. Formation of biotite rim, re-equilibration of micas and olivine breakdown (M.C. 2)

In the later stages of olivine-phlogopite micro-ijolite evolution, an Fe-rich and evolved melt formed, crystallizing the biotite rim around phlogopite phenocrysts that enclosed adjacent groundmass minerals (Figs. 4 and 9I). The phlogopite-biotite core-rim relationships appear to be a characteristic feature of Oldoinyo Lengai olivine-phlogopite micro-ijolites (Dawson et al., 1995; Sekisova et al., 2015). In pyroxenites, however, the biotite rim did not crystallize (Dawson and Smith, 1992a, b), suggesting that ijolite crystallization may be completed at lower temperatures than that of pyroxenites.

Re-equilibration of phlogopite phenocryst and biotite with the surrounding Ti-bearing minerals occurred at ~750 °C and ~650 °C, respectively. Thus, our data suggest that formation of olivine-phlogopite micro-ijolite terminated at depths of about 10–20 km. These depths are in accordance with seismic interpretations and elastic models suggesting a deep-seated magma chamber at about 15 km depth beneath Oldoinyo Lengai (Baer et al., 2008; Albaric et al., 2014; Weinstein et al., 2017).

As shown in Fig. 8, the majority of corona phlogopites failed to reach chemical equilibrium with surrounding Ti-bearing minerals, possibly leading to the formation of symplectites inside the double coronas (Fig. 5E and F). Most commonly, symplectites develop due to rapid mineral reactions, usually along decreasing temperature paths (Passchier and Trouw, 2005). Such a rapid temperature drop supports the extensive nucleation of the new mineral phases, since the nucleation rate is an exponential function of $\Delta T/\Delta t$ (cooling rate). Nevertheless, crystal growth rate and ΔT define a linear function leading to a very fine-grained microtexture. As titanite and olivine cannot be in equilibrium (Xirouchakis and Lindsley, 1998), they reacted to form symplectic microtextures of ilmenite and diopside (Fig. 9J), as shown in the following reaction:

$$FeMgSiO_4 \text{ (olivine)} + CaTiSiO_5 \text{ (titanite)} \rightarrow FeTiO_3 \text{ (ilmenite)} + CaMgSi_2O_6 \text{ (diopside)}$$

In the symplectite, zirconolite is a minor reaction product in addition to the major constituents, ilmenite and diopside (Fig. 5E and F). This mineral possibly acquired Zr released by the consumption of titanite (Tables 2 and 3). Titanite is in excess over olivine in the olivine-phlogopite micro-ijolites. Therefore, the presence of olivine (Fig. 5A)

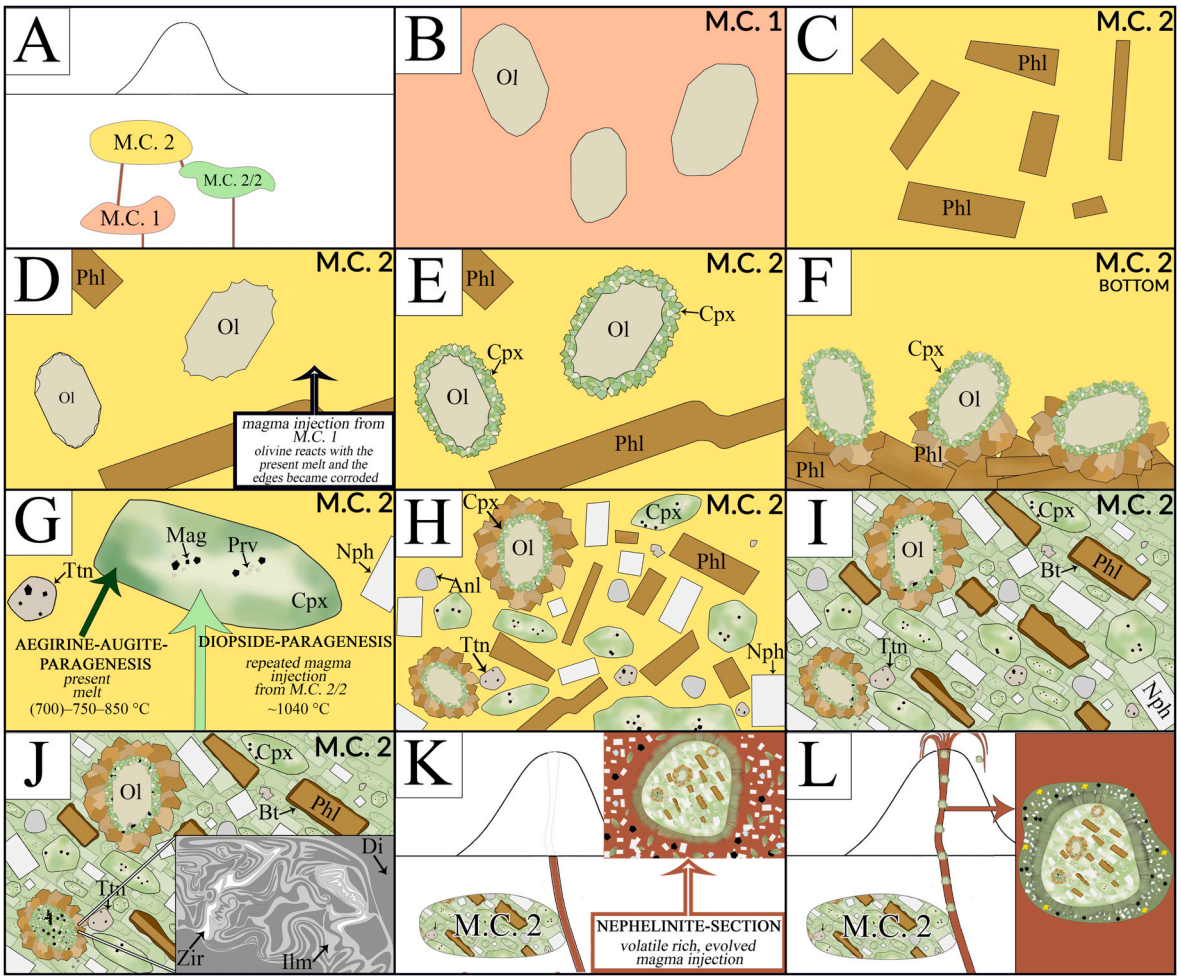

Fig. 9. Schematic flow chart showing the proposed evolution of the olivine-bearing ijolite from Oldoinyo Lengai. (A) Proposed magma chambers (MC); (B) MC-1 olivine crystallizes; (C) MC-2 phlogopite crystallizes and accumulates; (D) olivine-bearing magma transfers to MC-2, resulting in the formation of the corroded rim of olivine; (E) clinopyroxene crystallizes on corroded olivine; inner corona forms; (F) on the bottom of the magma chamber movements of olivine + clinopyroxene grains collect phlogopite crystal-cumulates; outer corona forms; (G) and (H) diopside and aegirine-augite crystallize alternately due to repeated magma impulses; groundmass minerals start to form; (I) biotite overgrows on phlogopite; olivine-phlogopite micro-ijolite forms; (J) formation of symplectites; (K) fragmentation of ijolite due to a contact with an evolved nephelinite melt, nephelinite starts to crystallize, clinopyroxene rim forms by the reaction between olivine-phlogopite micro-ijolite xenolith and nephelinite melt; (L) ijolite xenoliths are carried to the surface, during eruption glass and vesicles form. Abbreviations (Whitney and Evans, 2010): Ol – olivine, Phl – phlogopite, Cpx – clinopyroxene, Ttn – titanite, Mag – magnetite, Prv – perovskite, Nph – nepheline, Anl – analcime, Bt – biotite, Ilm – ilmenite, Di – diopside, Zir – zirconolite.

can be explained with double corona that mantled and protected olivines from symplectite-forming reactions. Larger olivine crystals (4 mm) with broad (2 mm) double corona (Fig. 5A and B) possibly had better opportunity to survive symplectitic alteration than smaller olivines mantled with a narrow double corona. This is supported by the existence of small («1 mm) double coronas (Fig. 5C) with ilmenite + diopside and without olivine in their core.

5.2.7. Nephelinite melt reaction with the ijolite (M.C. 2), eruption

The radially oriented clinopyroxene needles (Fig. 2C) between the olivine-phlogopite micro-ijolite xenolith and the nephelinite (Fig. 9K) suggest formation due to a contact metamorphic reaction. Such a reaction rim generally reflects rapid crystallization with heterogeneous nucleation (Vernon, 2004) as the hot nephelinite interacted with the olivine-phlogopite micro-ijolite.

The presence of wollastonite, aegirine-augite, Ti-andradite – schorlomite, Fe-bearing nepheline, Fe-rich and strongly peralkaline glass (Table 4, Fig. 6) and the absence of diopside and perovskite suggest an evolved, peralkaline and Fe-rich nature of the nephelinite host. This type of magma was commonly formed at Oldoinyo Lengai (Mitchell, 2009; Sharygin et al., 2012) and is considered representative of an evolved low-temperature magma (750–850 °C, Berkesi et al., 2020), sometimes enriched in volatiles. The absence of hydrous minerals in the nephelinite supports previous ideas of the predominance of CO_2 over H_2O in Oldoinyo Lengai evolved magmas (Dawson et al., 1995; Koepenick et al., 1996; Dawson, 2008; Berkesi et al., 2020). Wollastonite phenocrysts in nephelinite rocks from Oldoinyo Lengai usually are in places resorbed and have a combeite ($Na_2Ca_2Si_3O_9$) reaction rim. This textural feature is thought to develop due to a wollastonite-natrocarbonatite reaction with wollastonite resorption followed by combeite formation (Dawson, 1998, 2008; Sharygin et al., 2012). However, our fresh and uncorroded wollastonite (Fig. 6A and E) indicates this reaction did not occur in this sample. The olivine-phlogopite micro-ijolite xenoliths were transported to the surface by the nephelinite (Fig. 9L). The presence of glass in nephelinite suggests rapid quenching, whereas the vesicles suggest volatile exsolution (Fig. 6A–D).

6. Conclusions

Oldoinyo Lengai olivine-phlogopite micro-ijolites are

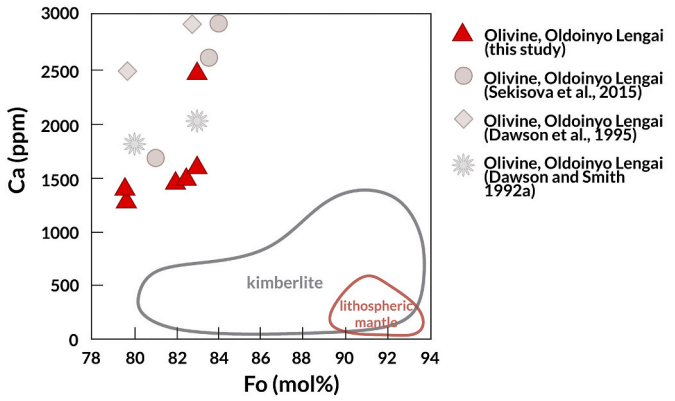

Fig. 10. Compositional differences of olivines formed in various geological environments shown on the Ca (ppm) – Fo (forsterite, mol%) diagram modified after Li et al. (2011). The ijolite-hosted olivines from Oldoinyo Lengai have a notably different composition than those from lithospheric mantle and kimberlites (Giuliani, 2018; Nowicki et al., 2008; Scott Smith et al., 2013), suggesting that these olivines precipitated from a mafic alkaline silicate melt rather than representing mantle fragments.

heterogeneous, complex rocks, containing a mixture of minerals crystallized at different stages during the evolution of an olivine-nephelinite parent magma. The olivines have low Mg# of 79–83 and 0.1–0.3 wt% CaO-content. Therefore, they are considered as the initial crystallization products and do not represent mantle fragments. Subsequent to its formation olivine is thought to have been transported to another magma chamber, resulting in its partial dissolution and the formation of a resorbed rim. This was followed by the crystallization of diopside during which the resorbed surface acted as the nucleus. Olivines, having diopside-coronas, possibly sank into phlogopite-rich crystal cumulate to form the typical double-corona texture. Subsequently, the groundmass characterized by diopside and perovskite (diopside paragenesis) was formed. Upon cooling of the magma, the diopside paragenesis was replaced by the aegirine-augite paragenesis crystallizing dominantly aegirine-augite and titanite. The coexistence of perovskite, titanite and nepheline in the groundmass permitted estimation of a maximum 1070–1040 °C temperature for its crystallization. Applying thermometers and homogenization temperature data, we independently estimated the formation temperatures for the diopside- and aegirine-augite paragenesis to be 970–1070 °C and 700–850 °C, respectively. The alternate zoning pattern of diopside and aegirine-augite in the groundmass clinopyroxene indicates an open plumbing system with several magma impulses during the formation of olivine-phlogopite micro-ijolite. We determined that the primary magmatic texture and mineral content of the olivine-phlogopite micro-ijolite changed, where olivine and titanite reacted to form a symplectite of ilmenite and diopside. Phlogopite phenocrysts show subsolidus re-equilibration with the coexisting perovskite, titanite, magnetite and zirconolite at ~750 °C and ~10–20 km depth.

We suggest that all rock-forming minerals in the olivine-phlogopite micro-ijolite have a magmatic origin and their formation was controlled by the state of the magma evolution coupled with magma mixing. With this statement we contradict and/or refute several earlier suggested genetic hypotheses. Our investigation might shed light on the importance of studying ilmenite + diopside symplectites, as these might infer the former presence of olivine in the parent magma of alkaline rocks, this mineral having possibility to be preserved during the evolution of magmas to higher SiO_2 activities in alkaline systems.

Funding

Tibor Guzmics reports financial support was provided by National Research Development and Innovation Office.

Declaration of competing interest

The authors declare that they have no known competing financial interests or personal relationships that could have appeared to influence the work reported in this paper.

Data availability

Data will be made available on request.

Acknowledgements

This study was supported by project NKFIH (National Research, Development, and Innovation Office of Hungary) K-119535 to T. Guzmics and M. Berkesi.

References

Albaric, J., Deverchere, J., Perrot, J., Jakovlev, A., Deschamps, A., 2014. Deep crustal earthquakes in North Tanzania, East Africa: interplay between tectonic and magmatic processes in an incipient rift. G-cubed 15, 374–394.
Babazadeh, S., Furman, T., Cottle, J.M., Raeisi, D., Lima, I., 2019. Magma chamber evolution of the Ardestan pluton, Central Iran: evidence from mineral chemistry, zircon composition and crystal size distribution. Mineral. Mag. 83 (6), 763–780.
Baer, G., Hamiel, Y., Shamir, G., Nof, R., 2008. Evolution of a magma-driven earthquake swarm and triggering of the nearby Oldoinyo Lengai eruption, as resolved by InSAR, ground observations and elastic modeling, East African Rift. Earth Planet Sci. Lett. 272, 339–352, 2007.
Baudouin, C., Parat, F., 2020. Phlogopite-olivine nephelinites erupted during early stage rifting, North Tanzanian divergence. Front. Earth Sci. 8, 277.
Beccaluva, L., Bianchini, G., Natali, C., Siena, F., 2017. The alkaline-carbonatite complex of Jacupiranga (Brazil): magma genesis and mode of emplacement. Gondwana Res. 44, 157–177.
Berkesi, M., Bali, E., Bodnar, R.J., Szabó, Á., Guzmics, T., 2020. Carbonatite and highly peralkaline nephelinite melts from Oldoinyo Lengai Volcano, Tanzania: the role of natrite-normative fluid degassing. Gondwana Res. 85, 76–83.
Brey, G., 1978. Origin of olivine melilitites—chemical and experimental constraints. J. Volcanol. Geoth. Res. 3, 61–88.
Brown, C., Girdler, R.W., 1980. Interpretation of african gravity and its implication for the breakup of the continents. J. Geophys. Res. 85, 6443–6455.
Carmichael, I.S.E., Nicholls, J., Smith, A.L., 1970. Silica activity in igneous rocks. Am. Mineral. 55, 246–263.
Carmody, L., 2012. Geochemical Characteristics of Carbonatite-Related Volcanism and Sub-volcanic Metasomatism at Oldoinyo Lengai, Tanzania. University College London [dissertation's thesis].
Clement, C.R., 1982. A Comparative Geological Study of Some Major Kimberlite Pipes in the Northern Cape and Orange Free State [dissertation's Thesis]. University of Cape, Town.
Dawson, J.B., Smith, J.V., 1988. Veined and metasomatised peridotite xenoliths from Pello Hill, Tanzania: evidence for anomalously light mantle beneath the Tanzania sector of the East African Rift Valley. Contrib. Mineral. Petrol. 100, 510–527.
Dawson, J.B., Smith, J.V., 1992a. Olivine-mica pyroxenite xenoliths from northern Tanzania: metasomatic products of upper-mantle peridotite. J. Volcanol. Geoth. Res. 50, 131–142.
Dawson, J.B., Smith, J.V., 1992b. Potassium loss during metasomatic alteration of mica pyroxenite from Oldoinyo Lengai, Northern Tanzania: contrast with fenitization. Contrib. Mineral. Petrol. 112 (2), 254–260.
Dawson, J.B., Smith, J.V., Steele, I.M., 1995. Petrology and mineral chemistry of plutonic igneous xenoliths from the carbonatite volcano, Oldoinyo Lengai, Tanzania. J. Petrol. 36, 797–826.
Dawson, J.B., 1998. Peralkaline nephelinite – natrocarbonetite relationships at Oldoinyo Lengai, Tanzania. J. Petrol. 39, 2077–2094.
Dawson, J.B., 1999. Melting and metasomatism in spinel peridotite xenoliths from Labait, Tanzania. In: Gurney, J.J., Gurney, J.L., Pascoe, M.D., Richardson, S.H. (Eds.), Proceedings of the 7th International Kimberlite Conference, 1. Red Roof Design, Cape Town, pp. 164–173.
Dawson, J.B., 2002. Metasomatism and partial melting in upper-mantle peridotite xenoliths from the Lashaine volcano, northern Tanzania. J. Petrol. 43, 1749–1777.
Dawson, J.B., 2008. The Gregory Rift Valley and Neogene-Recent Volcanoes in Northern Tanzania, vol. 33. Geological Society, London Memoir, pp. 64–66.
Dawson, J.B., 2012. Nephelinite-melilitite-carbonatite relationships: evidence from Pleistocene-recent volcanism in northern Tanzania. Lithos 152, 3–10.
de Moor, M., Fischer, T.P., King, P.L., Botcharnikov, R.E., Hervig, R.L., Hilton, D.R., 2013. Volatile-rich silicate melts from Oldoinyo Lengai volcano (Tanzania): implications for carbonatite genesis and eruptive behavior. Earth Planet Sci. Lett. 361, 379–390.
Ebinger, C.J., Sleep, N.H., 1998. Cenozoic magmatism throughout east-Africa resulting from impact of a single plume. Nature 395, 788–791.
Giuliani, A., 2018. Insights into kimberlite petrogenesis and mantle metasomatism from a review of the compositional zoning of olivine in kimberlites worldwide. Lithos 312, 322–342.

Green, D.H., 2015. Experimental petrology of peridotites, including effects of water and carbon on melting in the Earth's upper mantle. Phys. Chem. Miner. 42, 95–122.
Green, D.H., Falloon, T.J., Taylor, W.R., 1987. Mantle-derived magmas – roles of variable source peridotite and variable C–H–O fluid compositions. In: Mysen, B.O. (Ed.), Magmatic Process: Physicochemical Principles. Geochemical Geochemical Society Special Publication, pp. 139–154.
Grew, E.S., Locock, A.J., Mills, S.J., Galuskina, I.O., Galuskin, E.V., Hålenius, U., 2013. Nomenclature of the garnet supergroup. Am. Mineral. 98, 785–811.
Guzmics, T., Mitchell, R.H., Szabó, C.s., Berkesi, M., Milke, R., Ratter, K., 2012. Liquid immiscibility between silicate carbonate and sulfide melts in melt inclusions hosted in co-precipitated minerals from Kerimasi volcano (Tanzania): evolution of carbonated nephelinitic magma. Contrib. Mineral. Petrol. 164, 101–122.
Guzmics, T., Berkesi, M., Bodnar, R.J., Fall, A., Bali, E., Milke, R., Vetlényi, E., Szabó, C. s., 2019. Natrocarbonatites: a hidden product of three-phase immiscibility. Geology 47 (6), 527–530.
Hayden, L.A., Watson, E.B., Wark, D.A., 2007. A thermobarometer for sphene (titanite). Contrib. Mineral. Petrol. 155, 529–540.
Haslinger, E., Ottner, F., Lundström, U.S., 2007. Pedogenesis in the Alnö carbonatite complex, Sweden. Geoderma 142, 127–135.
Henry, D., Guidotti, C.V., Thomson, J., 2005. The Ti-saturation surface for low-to-medium pressure metapelitic biotites: implications for geothermometry and Ti-substitution mechanisms. Am. Mineral. 90, 316–328.
Kargin, A.V., Sazonova, L.V., Nosova, A.A., Lebedeva, N.M., Kostitsyn, Y.A., Kovalchuk, E.V., Tretyachenko, V.V., Tikhomirova, Y.S., 2019. Phlogopite in mantle xenoliths and kimberlite from the Grib pipe, Arkhangelsk province, Russia: evidence for multi-stage mantle metasomatism and origin of phlogopite in kimberlite. Geosci. Front. 10, 1941–1959.
Keller, J., Kraft, M., 1990. Effusive natrocarbonatite activity of Oldoinyo Lengai, june 1988. Bull. Volcanol. 52, 629–645.
Keller, J., Zaitsev, A., Wiedenmann, D., 2006. Primary magmas at Oldoinyo Lengai: the role of olivine melilitites. Lithos 91, 150–172.
Klaudius, J., Keller, J., 2006. Peralkaline silicate lavas at Oldoinyo Lengai, Tanzania. Lithos 91, 173–190.
Koepenick, K.W., Brantley, S.L., Thompson, J.M., Rowe, G.L., Nyblade, A.A., Moshy, C., 1996. Volatile emissions from the crater andflank of Oldoinyo Lengai volcano, Tanzania. J. Geophys. Res. 101, 13819–13830.
Li, C., Thakurta, J., Ripley, E.M., 2011. Low-Ca contents and kink-banded textures are not unique to mantle olivine: evidence from the Duke Island Complex, Alaska. Mineral. Petrol. 104, 147–153.
Lloyd, F.E., Bailey, D.K., 1975. Light element metasomatism of the continental mantle: the evidence and the consequences. Phys. Chem. Earth 9, 389–416.
McDonough, W.F., Rudnick, R.L., 1998. Mineralogy and composition of the upper mantle. Rev. Mineral. 37, 139–164.
Mitchell, R.H., 2009. Peralkaline nephelinite–natrocarbonatite immiscibility and carbonatite assimilation at Oldoinyo Lengai, Tanzania. Contrib. Mineral. Petrol. 158, 589–598.
Nielsen, T.F.D., Solovova, I.P., Veksler, I.V., 1997. Partial melts of melilitolite and origin of alkaline carbonatite: evidence from crystallised melt inclusions, Gardiner complex. Contrib. Mineral. Petrol. 126, 331–344.
Norry, M.J., Truckle, P.F.I., Lippard, S.J., Hawkesworth, C.J., Weaver, S.D., Marriner, G. F., 1980. Isotope and trace element evidence from lavas, bearing on mantle heterogeneity beneath Kenya. Philosophical Transactions of the Royal Society A 297, 259–271.
Nowicki, T., Porritt, L., Crawford, B., Kjarsgaard, B., 2008. Geochemical trends in kimberlites of the Ekati property, Northwest Territories, Canada: insights on volcanic and resedimentation processes. J. Volcanol. Geoth. Res. 174, 117–127.
Nyblade, A.A., 1997. Heat flow across the East african plateau. Geophys. Res. Lett. 24 (16), 2083–2086.
Passchier, C.W., Trouw, R.A.J., 2005. Microtectonics. Springer-Verlag, Berlin Heidelberg New York.
Peterson, T.D., Kjarsgaard, B.A., 1995. What are the parental magmas at Oldoinyo Lengai? In: Bell, K., Keller, J. (Eds.), Carbonatite Volcanism: Oldoinyo Lengai and the Petrogenesis of Natrocarbonatites, IAVCEI Proceedings in Volcanology 4, 148–162.
Pilipiuk, A.N., Ivanikov, V.V., Bulakh, A.G., 2001. Unusual rocks and mineralisation in a new carbonatite complex at Kandaguba, Kola Peninsula, Russia. Lithos 56, 333–347.
Putirka, K.D., 1996. Clinopyroxene + liquid equilibria to 100 kbar and 2450 K. Contrib. Mineral. Petrol. 135, 151–163.
Putirka, K.D., 2008. Thermometers and barometers for volcanic systems. Mineralogy & Geochemistry 69, 61–120.
Quennell, A.M., MCKinlay, A.C.M., Aitken, W.G., 1956. Part 1. Introduction and stratigraphy. Summary of the Geology of Tanganyika. Dar Es Salaam : Government Printer.
Reiss, M.C., Muirhead, J.D., Laizer, A.S., Link, F., Kazimoto, E.O., Ebinger, C.J., Rümpker, G., 2021. The Impact of Complex Volcanic Plumbing on the Nature of Seismicity in the Developing Magmatic Natron Rift, Tanzania. Front. Earth Sci. 8, 609805. https://doi.org/10.3389/feart.2020.609805.
Rezaei, M., Zarasvandi, A., 2019. Titanium-in-biotite thermometry in porphyry copper systems: challenges to application of the thermometer. Resour. Geol. 1–12.
Rogers, N., Macdonald, R., Fitton, G., George, R., Smith, M., Barreiro, B., 2000. Two mantle plumes beneath the East-African rift system: Sr, Nf, and Pb isotope evidence from Kenya Rift basalts. Earth Planet Sci. Lett. 176 (3–4), 387–400.
Savard, J.J., Mitchell, R.H., 2021. Petrology of ijolite series rocks from the Prairie Lake (Canada) and Fen (Norway) alkaline rock-carbonatite complexes. Lithos 396–397.
Scott Smith, B.H., Nowicki, T.E., Russell, J.K., Webb, K.J., Mitchell, R.H., Hetman, C.M., Harder, M., Skinner, E.M.W., Robey, J.A., 2013. Kimberlite terminology and classification. Proceedings of 10th International Kimberlite Conference, 2. Springer.
Sekisova, V.S., Sharygin, V.V., Zaitsev, A.N., Strekopytov, S., 2015. Liquid immiscibility during crystallisation of forsterite-phlogopite ijolites at Oldoinyo Lengai Volcano, Tanzania: study of melt inclusions. Russ. Geol. Geophys. 56, 1717–1737.
Sharygin, V.V., Kamenetsky, V.S., Zaitsev, A.N., Kamenetsky, M.B., 2012. Silicate–natrocarbonatite liquid immiscibility in 1917 eruption combeite–wollastonite nephelinite, Oldoinyo Lengai Volcano, Tanzania: melt inclusion study. Lithos 152, 23–39.
Simiyu, S., Keller, G.R., 1997. An integrated analysis of litospheric structure across the East-African plateau based on gravity anomalies and recent seismic studies. Techtonophysics 278, 291–313.
Simkin, T., Smith, J.V., 1970. Minor-element distribution in olivine. J. Geol. 78, 304–325.
Speer, J.A., 1984. Micas in igneous rocks. Rev. Mineral. 13, 229–356.
Veksler, I.V., Fedorchuk, Y.M., Nielsen, T.F.D., 1998a. Phase equilibria in the silica-undersaturated part of the KAlSiO4 ± Mg2SiO4 ± Ca2SiO4 ± SiO2 ± F system at 1 atm and the larnite-normative trend of melt evolution. Contrib. Mineral. Petrol. 131, 347–363.
Veksler, I.V., Nielsen, T.F.D., Sokolov, S.V., 1998b. Mineralogy of crystallized melt inclusions from gardiner and kovdor ultramafic alkaline complexes: implications for carbonatite genesis. J. Petrol. 39, 11–12, 2015–2031.
Vernon, R.H., 2004. Microstructures of igneous rocks. A practical guide to rock microstructure. Cambridge University Press.
Weinstein, A., Oliva, S.J., Ebinger, C.J., Roecker, S., Tiberi, Christel, et al., 2017. Fault-magma interactions during early continental rifting: seismicity of the Magadi-Natron-Manyara basins, Africa. Geochemistry, Geophysics, Geosystems, AGU and the Geochemical Society 18 (10), 3662–3686.
Whitney, D., Evans, B.W., 2010. Abbreviations for names of rock-forming minerals. Am. Mineral. 95, 185–187.
Woolley, A.R., Williams, C.T., Wall, F., Garcia, D., Moute, J., 1995. The Bingo carbonatite-ijolite-nepheline syenite complex, Zaire: geology, petrography, mineralogy and petrochemistry. J. Afr. Earth Sci. 21 (3), 329–348.
Woolley, A.R., Church, A.A., 2005. Extrusive carbonatites: a brief review. Lithos 85 (1), 1–14.
Woolley, A.R., Kjarsgaard, B.A., 2008. Paragenetic types of carbonatite as indicated by the diversity and relative abundance of associated silicate rocks: evidence from a global database. Can. Mineral. 46, 741–752.
Wölbern, I., Rümpker, G., Link, K., Sodoudi, F., 2012. Melt infiltration of the lower lithosphere beneath the Tanzania craton and the Albertine rift inferred from S receiver functions. G-cubed 13.
Xirouchakis, D., Lindsley, D.H., 1998. Equilibria among titanite, hedenbergite, fayalite, quartz, ilmenite, and magnetite: experiments and internally consistent thermodynamic data for titanite. Am. Mineral. 83, 712–725.
Yaxley, G.M., Anenburg, M., Tappe, S., Decree, S., Guzmics, T., 2022. Carbonatites: classification, sources, evolution, and emplacement. Annu. Rev. Earth Planet Sci. 50, 261–293.
Zurevinski, S.E., Mitchell, R.H., 2015. Petrogenesis of orbicular ijolites from the Prairie Lake complex, Marathon, Ontario: textural evidence from rare processes of carbonatitic magmatism. Lithos 239, 234–244.